Nano Research Energy

ISSN 2791-0091 CN 10-1944/O6
https://doi.org/10.26599/NRE.2026.9120254

Research Article

Solid-state ion plasticizer-engineered composite polymer electrolytes for high-voltage and wide-temperature lithium metal batteries

Qimin Peng[1], Yong Chen[2](✉), Jiajun Gong[1], Zhiye Hao[1], Guoxiu Wang[2], Shimou Chen[1](✉)

[1] State Key Laboratory of Chemical Resource Engineering, Beijing Key Laboratory of Electrochemical Process and Technology of Materials, Beijing University of Chemical Technology, Beijing 100029, China

[2] Centre for Clean Energy Technology, University of Technology Sydney, Broadway, Sydney, NSW 2007, Australia

Nano Research Energy, **Just Accepted Manuscript** • https://doi.org/10.26599/NRE.2026.9120254

https://www.sciopen.com/journal/2791-0091 on Jul. 15, 2026

Just Accepted

Table of Content

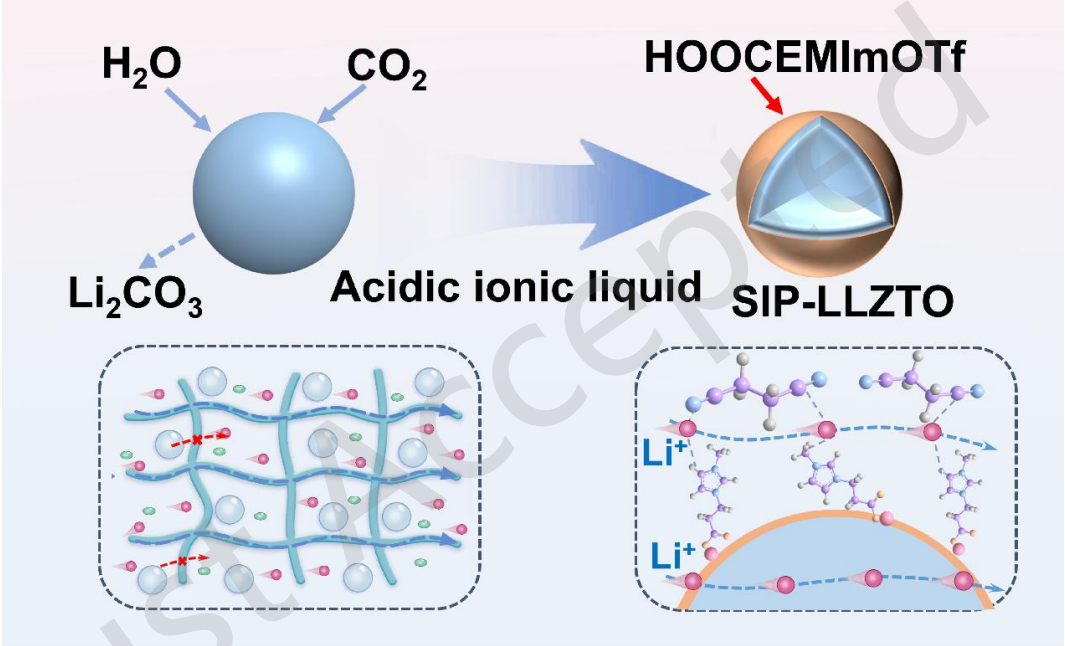

We developed an acidic ionic liquid interfacial modification strategy to engineer LLZTO as a solid inorganic plasticizer, which efficiently maintains rapid Li^+ conduction and unobstructed Li^+ transport pathways in composite solid electrolytes. Consequently, the resulting lithium metal batteries achieve stable cycling performance within a wide temperature range of −20 °C to 80 °C under high-voltage.

Nano Research Energy

ISSN 2791-0091 (print); 2790-8119 (online)

https://doi.org/10.26599/NRE.2026.9120254

Research Article

Solid-state ion plasticizer-engineered composite polymer electrolytes for high-voltage and wide-temperature lithium metal batteries

Qimin Peng[1], Yong Chen[2] (✉), Jiajun Gong[1], Zhiye Hao[1], Guoxiu Wang[2], and Shimou Chen[1] (✉)

[1]State Key Laboratory of Chemical Resource Engineering, Beijing Key Laboratory of Electrochemical Process and Technology of Materials, Beijing University of Chemical Technology, Beijing 100029, China

[2]Centre for Clean Energy Technology, University of Technology Sydney, Broadway, Sydney, NSW 2007, Australia

Received: 24 May 2026 / **Revised:** 17 June 2026 / **Accepted:** 30 June 2026

ABSTRACT

Composite polymer electrolytes (CPEs) offer a promising route toward practical lithium metal batteries. However, their performance in simple organic-inorganic composite systems remains limited. Herein, we engineer fast Li^+ conductor $Li_{6.4}La_3Zr_{1.4}Ta_{0.6}O_2$ (LLZTO) as a solid inorganic plasticizer (SIP) through interfacial modification with acidic ionic liquid (1-carboxyethyl-3-methylimidazolium trifluoromethanesulfonate). This design enables stable electrochemical performance in composite polymer electrolyte (CPE)-based high-voltage lithium-metal batteries (HV-LMBs) across a wide temperature range. Combined experimental and theoretical investigations demonstrate that the achieved wide-temperature stability stems from markedly enhanced composite compatibility and the construction of multidimensional ion-transport pathways. The SIP sustains efficiently fast Li^+ conduction at low temperatures and simultaneously preserves stable and unobstructed Li^+ transport pathways at elevated temperatures. Furthermore, the SIP significantly improves the membrane fracture strength and fracture strain compared with conventional organic-inorganic composites. Thus, the resulting CPEs enable wide-temperature stability of HV-LMBs paired with Ni-rich $LiNi_{0.8}Co_{0.1}Mn_{0.1}O_2$ cathodes over a range from −20 °C to 80 °C. This work effectively enhances the compatibility of organic-inorganic composites in CPEs by designing an ionic liquid interfacial layer, offering a new approach for developing CPEs-based HV-LMBs with high specific energy density and a wide operating temperature range.

Keywords: lithium metal batteries, solid inorganic plasticizer, composite polymer electrolytes, wide-temperature

Address correspondence to Yong Chen, yong.chen@student.uts.edu.au; Shimou Chen, chensm@buct.edu.cn

1 Introduction

With the rapid growth of the global electric

Nano Research Energy
ISSN 2791-0091 (print); 2790-8119 (online)
https://doi.org/10.26599/NRE.2026.9120254
Research Article

vehicle industry, conventional liquid lithium-ion batteries are becoming inadequate for next-generation power batteries owing to their limited energy density and the safety risks associated with flammable electrolytes [1–3]. By coupling a lithium metal anode with ultrahigh theoretical capacity (3860 $mAh \cdot g^{-1}$) and ultralow reduction potential (−3.04 V versus SHE) with nonflammable solid-state electrolytes (SSEs), solid-state lithium metal batteries (SSLMBs) are widely considered one of the most promising solutions for next-generation energy storage [4–7]. Typical SSEs primarily consist of inorganic solid electrolytes, solid polymer electrolytes, and composite polymer electrolytes (CPEs). Among these SSEs, CPEs have emerged as one of the most promising candidates for practical applications owing to their unique ability to combine the mechanical flexibility of polymers with the high ionic conductivity of inorganic solid electrolytes [8–10]. However, achieving wide-temperature operation remains challenging despite extensive research on CPE-based lithium metal batteries. The issue is further aggravated in high-voltage lithium metal batteries (HV-LMBs), a widely pursued battery configuration for achieving energy densities beyond 500 $Wh \cdot kg^{-1}$, because of their increased interfacial complexity [11, 12].

Simple organic-inorganic CPEs have been demonstrated to deliver only limited improvements in electrochemical performance. For example, although polyether-based poly(ethylene oxide) electrolytes have been extensively studied with a wide range of composite phases, their intrinsically sluggish ion transport and poor oxidative stability hinder their application in HV-LMBs [13, 14]. Fluorinated polymers, typically poly(vinylidene fluoride) (PVDF), have also been widely investigated. Extensive efforts have been devoted to regulating their polymer crystallization behavior through different residual solvents and fillers [15, 16]. Nevertheless, strategies based on residual-solvent regulation require precise control and still struggle to reconcile low-temperature ionic conductivity with chemical and electrochemical inertness at elevated temperatures. Although $Li_{6.4}La_3Zr_{1.4}Ta_{0.6}O_2$ (LLZTO) has been widely introduced into PVDF-based polymers, the resulting CPEs remain constrained by poor organic-inorganic compatibility at both the physical and chemical levels [17, 18]. LLZTO is prone to the formation of surface impurity phases, such as LiOH and Li_2CO_3, upon exposure to ambient air, which induces PVDF defluorination and disrupts CPE-based membrane homogeneity and ion-transport connectivity [19–21].

Surface modification of inorganic fillers has emerged as an effective strategy to improve interfacial compatibility in CPEs. For instance, Ma *et al.* [22] coated LLZTO with polydopamine, which can partially relieve interfacial stress, facilitate Li^+ transport, and guide uniform lithium deposition. Nevertheless, owing to the low ionic conductivity and limited

Nano Research Energy
ISSN 2791-0091 (print); 2790-8119 (online)
https://doi.org/10.26599/NRE.2026.9120254
Research Article

electrochemical stability of polydopamine, the overall ionic conductivity of the formed CPE was markedly compromised. Wu *et al.* [20] utilized phosphoric acid to modify LLZTO, which can effectively eliminate the surface alkaline impurity layer and improve the interfacial compatibility between the inorganic fillers and the polymer matrix. However, the interfacial adhesion strength between the inorganic acid-modified LLZTO and the polymer was weak, which readily induced interfacial delamination during long-term cycling. Furthermore, sluggish Li^+ conduction kinetics and non-uniform Li^+ flux give rise to severe instability at the electrolyte/anode interface, making it difficult to achieve homogeneous Li^+ deposition [23, 24]. Despite partial enhancement in ionic conductivity, the inorganic filler-polymer interface is still governed by physical interactions without continuous Li^+ pathways, resulting in high interfacial migration barriers and inferior performance at low temperatures and high current densities [25]. Zhang *et al.* [26] modified the polymer-LLZTO interface using isocyanate-propyl-triethoxysilane, which improved the particle dispersion uniformity in the CPE by 2-3 times. Thus, the introduction of organic modification layers has been shown to improve composite compatibility. Nevertheless, the limited ion-transport capability and thermal stability of most organic components have hindered their exploration in wide-temperature HV-LMBs, leaving the associated mechanisms largely unclear.

In this work, we report a solid inorganic plasticizer (SIP) engineering strategy for stable electrochemical performance in CPE-based HV-LMBs across a wide temperature range. As a representative demonstration, a typical CPE composed of fast Li^+ conductor LLZTO and PVDF-HFP was employed, in which ionic-liquid-modified LLZTO serves as the SIP. Experimental observations supported by theoretical calculations demonstrate that the wide-temperature stability is governed by enhanced composite compatibility and multidimensional ion-transport pathways. The SIP maintains efficient Li^+ conduction at low temperature (−20 °C) and preserves stable ion transport at the elevated temperature (80 °C). The proposal electrolyte delivered a high ionic conductivity of 4.72×10^{-4} $S\cdot cm^{-1}$ and Li^+ transference number of 0.59 at room temperature (RT). Furthermore, it yields nearly a twofold improvement in both fracture strength and fracture strain relative to conventional organic-inorganic composites. Thus, the resulting CPEs enable the Li||Li symmetric cells to achieve a high critical current density (CCD) of 1.8 $mA\cdot cm^{-2}$ and exhibit stable long-term galvanostatic cycling for more than 2100 h at 0.1 $mA\cdot cm^{-2}$. Benefiting from these merits, assembled Li||NCM811 full cells can stably cycle over 250 cycles with a capacity retention of up to 99.5% at RT. In addition, the full cells maintained stable operation over 400 cycles and 310 cycles at high temperature of 60 ° C and low temperature of −10 °C, respectively, presenting

Nano Research Energy
ISSN 2791-0091 (print); 2790-8119 (online)
https://doi.org/10.26599/NRE.2026.9120254
Research Article

exceptional cycling stability. This work presents a promising route for inorganic nanocomposite design based on surface ionic liquid layers, providing a facile and effective strategy for developing high performance CPEs for HV-LMBs with high safety, high energy density, and wide-temperature applicability.

2 Results and discussion

2.1 SIP engineering design and its influence on CPE

Fast Li^+ condutor LLZTO readily forms ion-transport-inactive surface layers of Li_2CO_3 and LiOH [20]. To remove these impurities and facilitate Li^+ transport across the composite organic/inorganic interface in a typical LLZTO/PVDF-HFP CPE (hereafter denoted as PHL), an acidic ionic liquid, 1-carboxyethyl-3-methylimidazolium trifluoromethanesulfonate, was introduced to generate a uniform and compact modified layer on LLZTO, yielding the target CPE (hereafter denoted as CPHL) (Fig. 1(a)). X-ray diffraction (XRD) results of pristine LLZTO exhibited a pronounced diffraction peak at $2\theta \approx 21°$ (Fig. 1(b)), which is assigned to crystalline Li_2CO_3 impurities [27]. By contrast, this impurity peak disappeared in SIP-LLZTO, confirming effective surface impurity removal without significantly altering the fast-ion-conducting phase of the LLZTO filler. This observation was further supported by X-ray photoelectron spectroscopy (XPS) (Fig. S1 in the Electronic Supplementary Material (ESM)). These results indicated that the acidic ionic liquid mediated the *in situ* conversion of the Li_2CO_3 layer into an ionic-liquid-derived interfacial architecture. The transformation not only alleviated the interfacial incompatibility between LLZTO and the polymer matrix, but also built a percolating network for efficient Li^+ ions transport, enhancing the overall ionic conductivity of the composite electrolyte.

Imidazolium-based ionic liquids were selected because they combine good compatibility with the PVDF-HFP matrix [28], favourable $LiNO_3$ dissociation behaviour, and superior physicochemical stability. Their compatibility with PVDF-HFP arised from favourable interactions between the imidazolium cations and fluorine atoms along the polymer chains. Scanning electron microscopy (SEM) and energy-dispersive X-ray spectroscopy (EDS) elemental mapping confirmed that the excellent compatibility between SIP-LLZTO and PVDF-HFP, enabling the CPHL membrane with a homogeneous morphology, along with the uniform distribution of La, Zr, and Ta elements throughout the membrane (Figs. 1(c) and 1(d) and Fig. S2 in the ESM). By contrast, PHL showed pronounced LLZTO nanoclusters and dense crystallization (Figs. 1(e) and 1(f) and Fig. S3 in the ESM). Cross-sectional SEM characterization confirmed that the as-prepared comosite electrolyte membrane has a uniform thickness of approximately 44 μm (Fig. S4 in the ESM). Small-angle X-ray scattering (SAXS) analysis reveals the nanoscale structural evolution of the composite electrolytes (Fig. 1(g)). The absence of distinct

Nano Research Energy
ISSN 2791-0091 (print); 2790-8119 (online)
https://doi.org/10.26599/NRE.2026.9120254
Research Article

scattering features related to phase separation indicates good interfacial compatibility between the fillers and the PVDF-HFP matrix. Compared with PHL, the stronger low-Q scattering of CPHL suggests enhanced electron-density contrast and reinforced interactions at the SIP-LLZTO/PVDF-HFP interface. The nearly overlapping high-Q profiles further indicate that ionic liquid modification mainly regulates the filler-polymer interfacial microstructure without significantly changing the intrinsic chain packing of PVDF-HFP. This uniform and strengthened nanocomposite structure provides a favorable framework for high-flux Li^+ transport [9]. XRD patterns of the PHL and CPHL membranes further showed that the incorporation of SIP-LLZTO markedly suppressed the crystalline peaks of PVDF-HFP, in which the reduced crystallinity facilitated efficient Li^+ migration (Fig. S5 in the ESM) [28]. Although PHL also showed no obvious phase separation, significant defluorination was observed in the control membrane (Fig. 1(h) and Fig. S6 in the ESM), whereas CPHL exhibited no evident chemical decomposition. The desorption-induced formation of C=C bonds was clearly detected by FTIR, with a characteristic band at 1666 cm^{-1} [9]. Atomic force microscopy (AFM) results corroborate the SEM observations, with the flat and homogeneous surface morphology of the CPHL membrane confirmed the excellent compatibility between SIP-LLZTO and the PVDF-HFP matrix (Fig. S7 in the ESM). The electrolyte morphology further influences the mechanical properties of the membrane. Mechanical testing showed that the CPHL membrane exhibited a Young's modulus of 2.9 GPa, substantially higher than that of PHL (1.9 GPa) (Fig. 1(i) and Fig. S8 in the ESM). Moreover, the CPHL electrolyte exhibited excellent mechanical flexibility and can be bent into various shapes without any visible surface cracks (Fig. S9 in the ESM). Tensile tests further showed that the CPHL membrane delivered a fracture strength of 6.7 MPa and a fracture strain of approximately 190%, confirming its markedly improved mechanical performance relative to the PHL electrolyte (Fig. 1(j)).

Furthermore, the acidic ionic-liquid-modified LLZTO showed favourable solid-state stability and good dispersibility, rendering it a promising candidate for SIPs (Fig. 1(c) and Fig. S6 in the ESM). The stability of CPHL was also assessed by thermogravimetric analysis (TGA) and flammability tests (Fig. 1(k) and Fig. S10 in the ESM), confirming the favourable solid-state stability of SIP.

To confirm the beneficial role of SIP in promoting ion transport within CPHL, the temperature-dependent ionic conductivity was evaluated (from 25 °C to 70 °C). The results exhibited that the CPHL possessed a higher ionic conductivity of 4.72×10^{-4} $S \cdot cm^{-1}$ compared with the PHL (3.64×10^{-4} $S \cdot cm^{-1}$) at room temperature (RT) (Fig. 2(a), Figs. S11 and S12 in the ESM). The activation energy for

Nano Research Energy
ISSN 2791-0091 (print); 2790-8119 (online)
https://doi.org/10.26599/NRE.2026.9120254
Research Article

ion-transport was determined by fitting the Arrhenius equation. The CPHL delivered the lowest activation energy (6.72 kJ·mol^{-1}) than PHL (7.18 kJ·mol^{-1}). It indicated reduced transport barriers and enhanced ion mobility [29]. Furthermore, the ion conductivity of CPHL electrolyte was similar at low temperatures, and its high-temperature performance was significantly improved (Fig. S13 in the ESM). The reduced Li^+ migration barrier indicates lower internal resistance and more efficient Li^+ transport enabled by the modified ionic-liquid layer on the LLZTO surface. Li^+ transference numbers (t_{Li^+}) of PHL and CPHL were 0.38 and 0.59, respectively (Fig. 2(b) and Fig. S14 in the ESM). The higher t_{Li^+} of CPHL was mainly attributed to the conversion of insulating surface impurities into a multifunctional interfacial layer that enables ion screening and promotes Li^+ transport, markedly enhancing Li^+ -transport efficiency. The comprehensive ^7Li solid-state nuclear magnetic resonance (NMR) spectroscopy (Fig. 2(c)) revealed a downfield shift in the Li^+ resonance upon SIP-LLZTO addition, demonstrating reduced local electron density and a modified Li^+ coordination environment, confirming that CPHL promoted lithium salt dissociation and facilitates Li^+ mobility [30, 31].

Nano Research Energy

ISSN 2791-0091 (print); 2790-8119 (online)

https://doi.org/10.26599/NRE.2026.9120254

Research Article

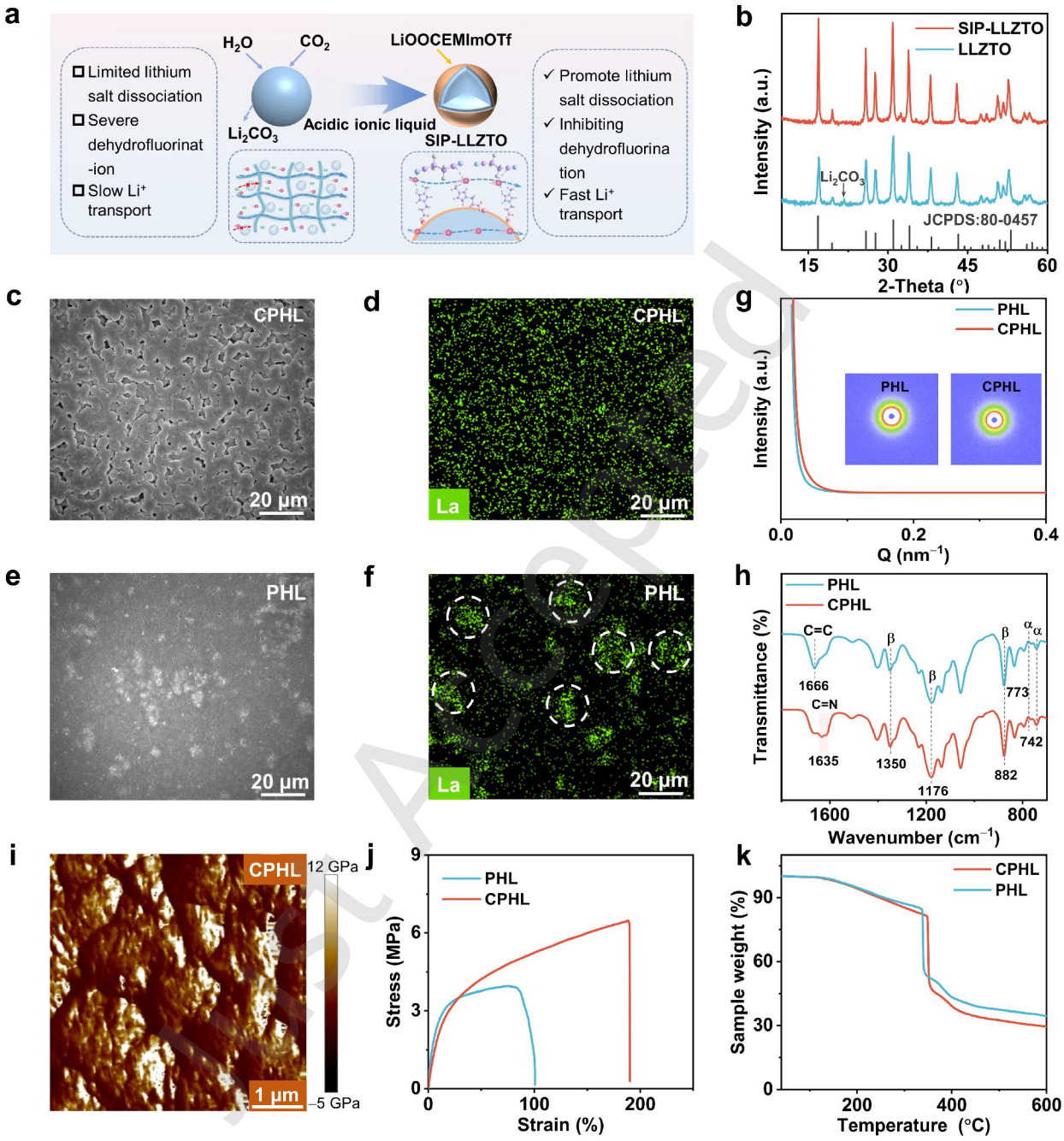

Figure 1 (a) Schematic illustration of rapid Li^+ conduction enabled by solid inorganic plasticizers in polymer electrolytes. (b) XRD patterns of SIP-LLZTO and LLZTO. (c) SEM image of CPHL electrolyte. (d) EDS mapping of CPHL. (e) SEM image of PHL electrolyte. (f) EDS mappings of PHL. (g) SAXS of PHL and CPHL electrolytes. (h) FTIR spectra. (i) Young's modulus of CPHL membrane. (j) Stress-strain curves of PHL and CPHL electrolytes. (k) TGA curves of PHL and CPHL.

Changes in Li^+ solvation structure were probed by Raman spectroscopy. As shown in Figs. 2(d) and 2(e), Raman spectra of CPHL and PHL were analyzed in 730–770 cm^{-1}. Deconvolution of the peak produced three peaks with wave number of 741, 745, and 752

Nano Research Energy

ISSN 2791-0091 (print); 2790-8119 (online)

https://doi.org/10.26599/NRE.2026.9120254

Research Article

cm^{-1}, attributed to solvent separated ion pair (SSIP), contact ion pair (CIP), and aggregate (AGG), respectively. The peak proportion at 741 cm^{-1} for CPHL and PHL is 30% and 13.7%, respectively, indicating the highest proportion of free $TFSI^-$ and the lowest proportion of Li^+-$TFSI^-$ ion cluster in the

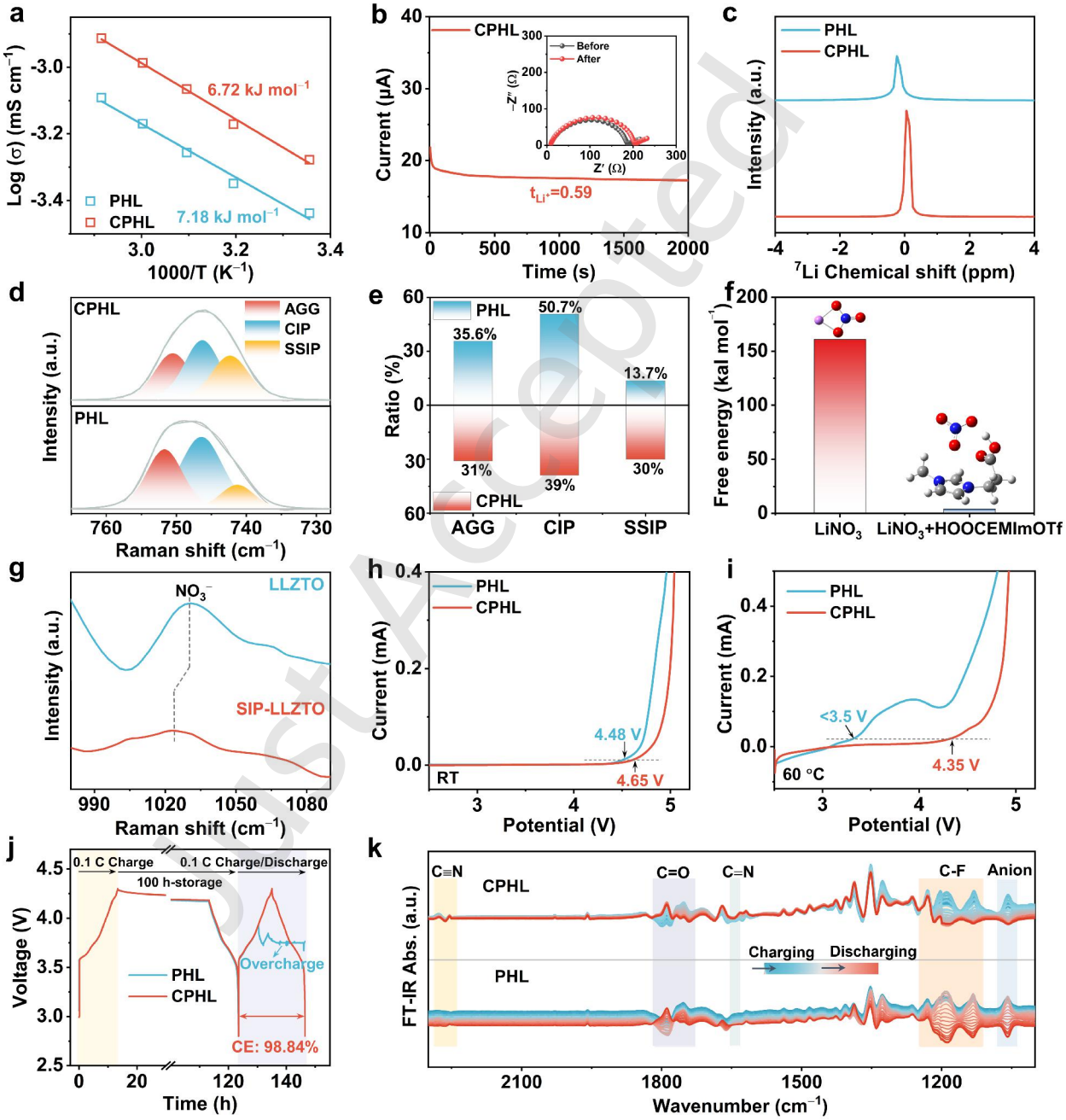

Figure 2 (a) Activation energies of PHL and CPHL. (b) Li^+ ion transference number of CPHL. (c) Solid-state ^7Li NMR of PHL and CPHL. (d) Raman spectra of $TFSI^-$ in PHL and CPHL. (e) Proportion of AGGs, CIP, and SSIP in Raman spectra. (f) Free energy of Li^+-NO_3^- and $LiNO_3$+HOOCEMImOTf. (g) Raman spectra of NO_3^- of LLZTO and SIP-LLZTO immersed LE (LiTFSI: PC:SN=1:3:3, 0.5 wt.% $LiNO_3$). LSV of PHL and

Nano Research Energy
ISSN 2791-0091 (print); 2790-8119 (online)
https://doi.org/10.26599/NRE.2026.9120254
Research Article

CPHL at (h) RT and (i) 60 °C. (j) Columbic efficiency and self-discharge profiles of Li||NCM811 cells. (k) *In-situ* FTIR monitoring of the PHL and CPHL at the cathode.

favourable conditions for the formation of efficient Li^+ conduction pathways [34]. Calculations further confirmed that the imidazolium cation significantly promotes $LiNO_3$ dissociation, supporting its function as an effective additive for the lithium-metal anode (Fig. 2(f)). Raman spectroscopy of the $LiNO_3$-containing electrolyte further confirmed that SIP-LLZTO promoted $LiNO_3$ dissolution [35]. As shown in Fig. 2(g), SIP-LLZTO incorporation induced an attenuated and broadened nitrate-related Raman band with a clear upshift, revealing a perturbed NO_3^- coordination environment and promoted $LiNO_3$ dissociation [36].

Moreover, compared with conventional organic and siloxane modifications, ionic-liquid modification promoted ion transport and provided excellent thermal and electrochemical stability (Fig. S15 in the ESM). To evaluate the high-voltage and high-temperature feasibility of incorporating the SIP into CPHL, we carried out a comparative study using the conventional PHL system as a reference. As shown in Figs. 2(h) and 2(i), linear sweep voltammetry (LSV) measurements at different temperatures revealed that CPHL delivered a wider electrochemical stability window at RT and elevated temperatures. Notably, even at 60 °C, CPHL maintained an electrochemical window of up to 4.35 V, which was sufficient to meet the operating requirements of Ni-rich cathodes. Imidazole ionic liquid modified LLZTO can not only remove catalytic impurities such as LiOH and Li_2CO_3 on its surface, but also construct a high-pressure resistant organic interface layer and improve compatibility with PVDF-HFP matrix, suppressing various interface and matrix side reactions at high temperatures. To evaluate the long-term interfacial stability under high-voltage conditions, the self-discharge behavior of the cells was investigated at a cutoff voltage of 4.3 V. As depicted in Fig. 2(j), the CPHL cell not only exhibited reduced voltage decay after 100 h of rest but also delivered an exceptional coulombic efficiency of 98.84% upon subsequent cycling, significantly outperforming PHL.

In situ FTIR analysis provided further insight into the cathode-side interfacial evolution enabled by SIP engineering. Difference spectra collected during galvanostatic charge-discharge of Li||NCM811 full cells were analyzed to compare the high-voltage interfacial chemistry of CPHL and PHL. Fig. 2(k) showed that the variation of the infrared peak in the range of 1040–1080 cm^{-1} was unique to $TFSI^-$ anions, and CPHL always displayed a positive peak on the cathode during charging and a negative peak during discharging. This opposite reaction arose from the solvation and desolvation of Li^+ ions. Compared with PHL, the characteristic peaks of C=N (2276 cm^{-1}) and C=O (1800–1850 cm^{-1}) in CPHL did not show significant

Nano Research Energy
ISSN 2791-0091 (print); 2790-8119 (online)
https://doi.org/10.26599/NRE.2026.9120254
Research Article

changes during the charging process, indicating that CPHL effectively maintained the structural stability of the electrolyte under high voltage conditions [37, 38]. These results confirmed that the introduction of SIP-LLZTO effectively stabilized the interface between the polymer matrix, inhibiting the excessive electrolyte decomposition, illustrating superior interfacial chemical stability.

2.2 Evaluation of interface compatibility with lithium metal anode

To further verify the compatibility between CPEs and Li metal anodes, Li||Li symmetric cells were cycled under a current density of 0.1 mA·cm^{-2} with a capacity of 0.1 mAh·cm^{-2} (Fig. 3(a)). For the Li | PHL | Li cell, the Li plating/stripping voltage increased considerably with prolonged cycling. After approximately 560 h of cycling, the PHL-based cell experienced a short circuit, indicating the cell failure. The phenomenon was attributed to the continuous growth of lithium dendrites and the insufficient dendrite-inhibiting capability of the PHL electrolyte. In contrast, the CPHL-based symmetric cell exhibited a stable and low overpotential without any short-circuit behavior even after 2100 h.

Furthermore, the critical current density (CCD) of Li||Li symmetric cells using CPHL reached 1.8 mA·cm^{-2}, higher than that of PHL (1.3 mA·cm^{-2}) (Fig. 3(b)), indicating the excellent Li stripping/plating kinetics. The Li | CPHL | Li symmetric cell still delivered outstanding Li plating/stripping cycling even at high current densities of 0.2 and 0.5 mA·cm^{-2} (Fig. 3(c) and Fig. S16 in the ESM). The Tafel curves in (Fig. S17 in the ESM) illustrated that the CPHL exhibited a higher exchange current density of 0.359 mA·cm^{-2} than that of the PHL (0.252 mA·cm^{-2}), which indicated an enhancement Li^+ transport kinetics. To elucidate the dynamic evolution of interfacial and bulk properties during electrochemical operation, *in situ* electrochemical impedance spectroscopy (EIS) was conducted over multiple cycling intervals. The charge transfer resistance (R_{ct}) decreased after the initial cycle and stabilized with continued cycling, indicating that the formation of a robust and highly conductive solid electrolyte interface (SEI). In contrast, PHL exhibited a continuous increase in both R_{ct} and interfacial resistance upon cycling, reflecting persistent structural and chemical degradation (Fig. S18 in the ESM). This was mainly ascribed to the progressive dehydrofluorination of PVDF-HFP and the decomposition of the LLZTO interface induced by residual DMF solvent. Distribution of relaxation times (DRT) analysis provided further insights into interfacial kinetics. In CPHL system, the characteristic peaks related to SEI and R_{ct} rapidly stabilized within the initial few cycles, indicating that the interface quickly reached a steady state with minimal fluctuation [39]. Benefiting from the effective ion conduction of SIP-LLZTO, the compatibility with polymers was improved. In contrast, the impedance signal corresponding to SEI in the PHL system increased continuously, reflecting increasingly severe interfacial

Nano Research Energy

ISSN 2791-0091 (print); 2790-8119 (online)

https://doi.org/10.26599/NRE.2026.9120254

Research Article

heterogeneity and instability (Figs. 3(d) and 3(e)). SEM images were used to investigate the dendrite growth and deposition behavior of various electrolytes during cycles. As depicted in Figs. 3(f) and 3(g), when employed the PHL electrolyte, distinct dendritic structures and dead lithium formation were observed on the lithium metal surface. In contrast, after applied the CPHL electrolyte, the lithium metal surface exhibited a smooth morphology, with no evidence of dendrite formation.

To elucidate the enhanced interface compatibility and stability, XPS spectroscopy was used to analyze the mechanisms underlying the interfacial stability of CPEs with the Li metal anode. As shown in Figs. 3(h) and 3(i) and Fig. S19 in the ESM, the SEI layer formed on the Li anode surface during cell cycling was primarily composed of organic-C components and inorganic species, which originated from the decomposition of residual DMF solvent and lithium salts [40].

Nano Research Energy

ISSN 2791-0091 (print); 2790-8119 (online)

https://doi.org/10.26599/NRE.2026.9120254

Research Article

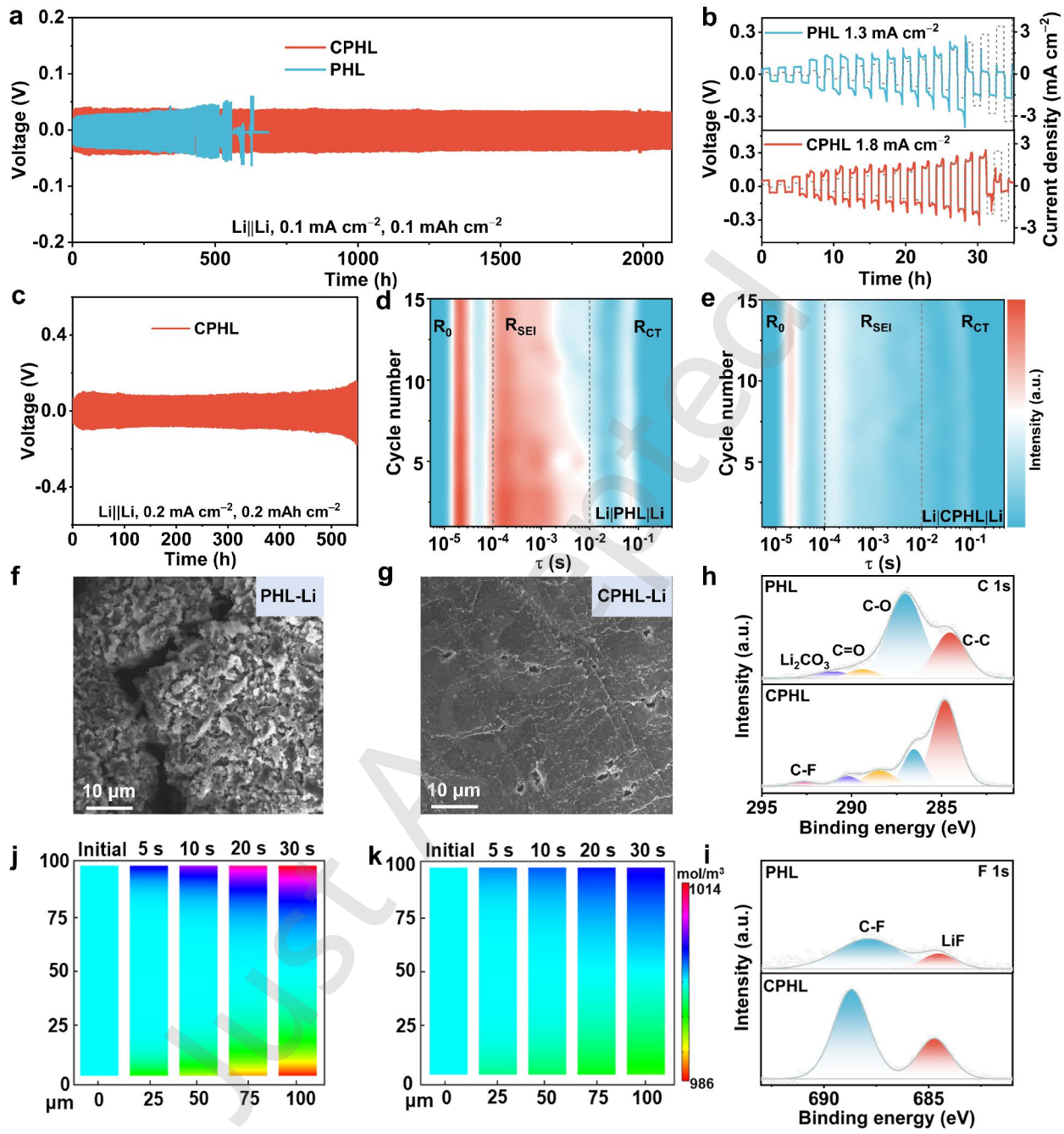

Figure 3 (a) Galvanostatic cycling curves of Li||Li symmetric cells using PHL and CPHL at 0.1 mA·cm^{-2} and 0.1 mAh·cm^{-2}. (b) Critical current density of Li||Li symmetric cells. (c) Galvanostatic cycling curves of Li||Li symmetric cells using PHL and CPHL at 0.2 mA·cm^{-2} and 0.2 mAh·cm^{-2}. DRT mapping diagrams of (d) Li|PHL|Li and (e) Li|CPHL|Li symmetric cells at different cycles. SEM images of the Li metal anodes after cycling in (f) PHL and (g) CPHL. XPS spectra of (h) C 1s and (i) F 1s on the Li metal anodes after cycling with different electrolytes. COMSOL Multiphysics FEMS results of the Li^+ concentration distribution based

Nano Research Energy

ISSN 2791-0091 (print); 2790-8119 (online)

https://doi.org/10.26599/NRE.2026.9120254

Research Article

on (j) Li|PHL|Li and (k) Li|CPHL|Li symmetric cells.

Notably, compared to the PHL electrolyte, the SEI layer formed on the lithium metal anode in the Li | CPHL | Li symmetric cell exhibited a lower content of organic components and Li_2CO_3, along with a higher content of LiF. As a key inorganic component of the SEI, LiF facilitated the Li^+ transport through the SEI layer, effectively suppressed lithium dendrite growth, and enhanced the stability of the electrode/electrolyte interface [19, 41].

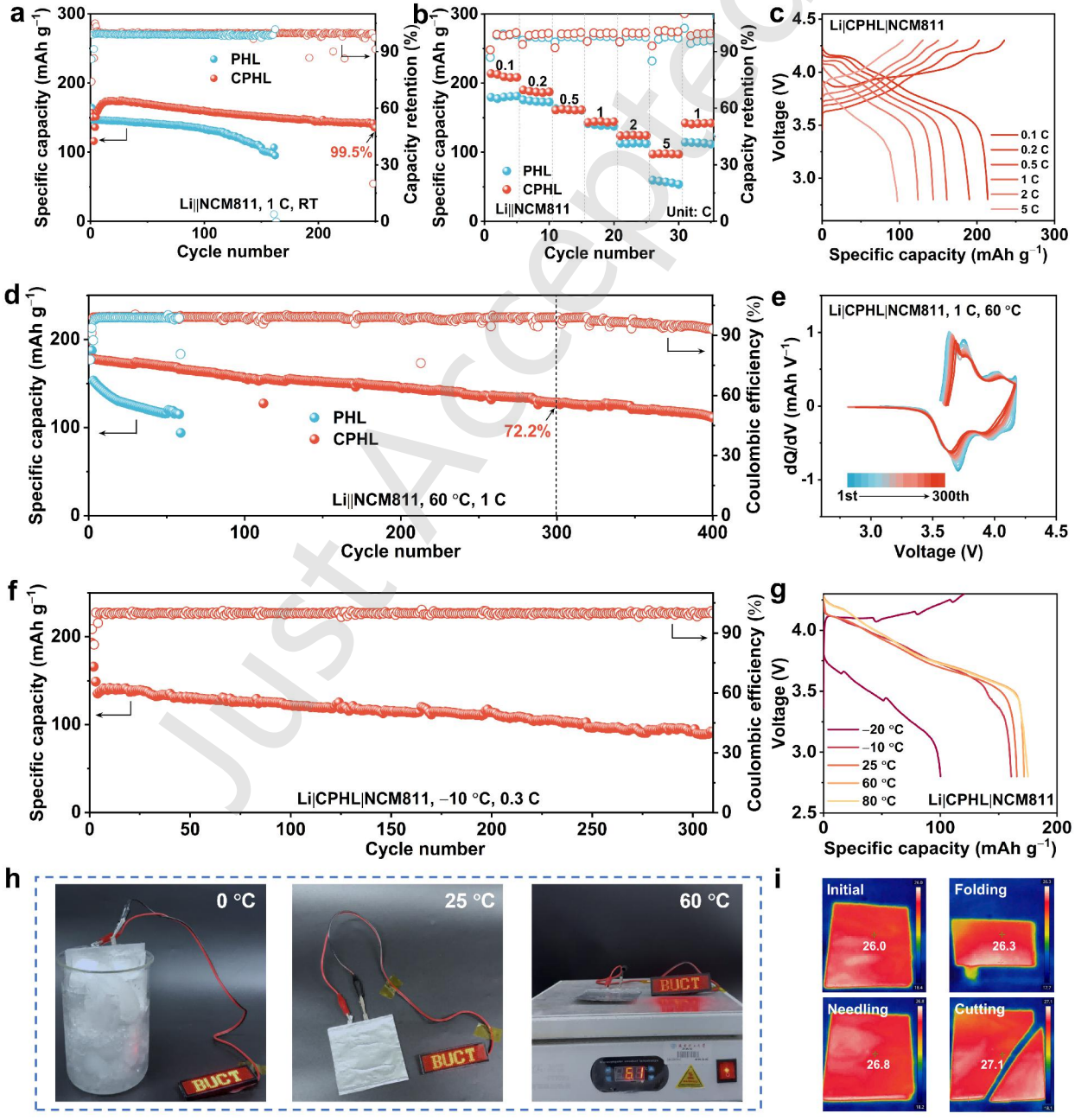

Figure 4 (a) Long-term cycling performance of Li | | NCM811 cells at 1 C and 2.8–4.3 V. (b) Rate

Nano Research Energy
ISSN 2791-0091 (print); 2790-8119 (online)
https://doi.org/10.26599/NRE.2026.9120254
Research Article

performance of the Li||NCM811 cells based on PHL and CPHL. (c) Charge/discharge profiles of Li|CPHL|NCM811 cell at different current densities. (d) The cycling performance of Li|CPHL|NCM811 cell at 1 C and 60 °C. (e) The dQ/dV curves of Li||NCM811 cells at 60 °C. (f) The cycling performance of Li|CPHL|NCM811 cell at 0.3 C and −10 °C. (g) Charge/discharge profiles of Li|CPHL|NCM811 full cell at different temperatures. (h) Pictures of Li|CPHL|NCM811 pouch cell light the LED panel at different temperatures. (i) Infrared thermal imaging photographs of Li|CPHL|NCM811 pouch cell under abuse conditions.

In addition, finite-element method simulations (FEMS) using COMSOL Multiphysics further quantified the interfacial stability. As shown in Figs. 3(j) and 3(k), CPHL exhibited smaller concentration gradients of Li^+ during plating/stripping compared to PHL. In summary, the high t_{Li^+} and the rapid ion transport mechanism in CPHL work synergistically to effectively alleviate Li^+ ions concentration polarization at the interface and optimize the electric field distribution, inhibiting the formation of lithium dendrites [42, 43]. It enabled high-voltage lithium metal batteries employing CPHL electrolytes to exhibit outstanding electrochemical performance and long-term cycling stability.

2.3 Full-cell performance under wide-temperature conditions

The electrochemical performance of PHL and CPHL in a practical cell system was systematically evaluated using $LiFeO_4$ (LFP) and high-voltage $LiNi_{0.8}Co_{0.1}Mn_{0.1}O_2$ (NCM811) cathodes.

As shown in Fig. S20 in the ESM, Li|CPHL|LFP cells exhibited an excellent rate performance (162.2 mAh·g^{-1} at 0.1 C, 100.4 mAh·g^{-1} at 5 C), outperforming to that of Li|PHL|LFP cells (141.3 mAh·g^{-1} and 29.5 mAh·g^{-1}). Furthermore, when the current density was restored to 1 C, the specific capacity of Li|CPHL|LFP recovered to 98.6% of its initial value, demonstrating favorable reversibility. This was attributed to the excellent conductivity of SIP-LLZTO in the CPHL electrolyte, which improved the interfacial compatibility with both lithium metal anode and LFP cathode, significantly reducing the interface charge transfer resistance and accelerating the overall cell reaction kinetics. Additionally, long-term cycling tests of Li||LFP cells were also conducted. The Li||LFP cells employing CPHL showed stable cycling over 500 cycles with an average coulombic efficiency of 99.81% and a high-capacity retention of 91.4% at 1 C. In comparison, the capacity of the cell based on PHL decreased to 53.8% after 217 cycles (Fig. S21 in the ESM). This performance difference can be mainly ascribed to two factors: the reduced ionic conductivity caused by the agglomeration of LLZTO particles, and the conductivity degradation arose from the instability of PHL electrolyte.

Impressively, the Li|CPHL|LFP cell still exhibited outstanding cycling stability even when the current density was increased to 3 C

Nano Research Energy
ISSN 2791-0091 (print); 2790-8119 (online)
https://doi.org/10.26599/NRE.2026.9120254
Research Article

and coupled with a high-loading cathode (9 mg·cm^{-2}) (Figs. S22 and S23 in the ESM). To evaluate the high-voltage stability, the chemically aggressive NCM811 cathode was used. As depicted in Fig. 4(a), the Li | CPHL | NCM811 cells showed a stable cycling performance, maintaining 99.5% of its initial capacity after 250 cycles. In contrast, the Li|PHL|NCM811 cells exhibited rapid capacity decay and showed pronounced degradation observed after 150 cycles. Moreover, the Li | CPHL | NCM811 cell delivered impressive rate capacities of 213.78 to 97.13 mAh·g^{-1} at ranging from 0.1 to 5 C, with a charge cut-off voltage of 4.3 V. At the same time, when the current density was restored to 1 C, the full cell demonstrated favorable capacity recovery characteristics (Fig. 4(b, c)). When the cathode loading of NCM811 increased to 11.4 mg·cm^{-2}, the Li | CPHL | NCM811 cells still exhibited excellent stability even after cycling at 0.1 C (Fig. S24 in the ESM). The cyclic voltammetry (CV) curves of the Li|CPHL|NCM811 cell revealed its superior electrochemical reversibility (Fig. S25 in the ESM) [44]. In addition, to extend the operational temperature window of the cell, the electrochemical performance of the Li||NCM811 cell employed this electrolyte was further evaluated over a wide temperature range (−10 °C to 60 °C). As depicted in Fig. 4(d) with the operating temperature was raised to 60 °C, the Li | CPHL | NCM811 cells achieved higher capacity retention rates of 72.2% after 300 cycles at 1 C with a cut-off voltage of 4.2 V. By contrast, the Li||NCM811 full cells assembled based on the PHL electrolyte exhibited overcharging and the cell failure after 50 cycles at 60 °C. The dQ/dV profiles of the Li|CPHL|NCM811 full cells showed highly symmetric peaks with negligible shift over 300 cycles (Fig. 4(e)), confirming that the CPHL electrolyte effectively suppresses interfacial side reactions and enables stable reaction kinetics with excellent cycling reversibility. In terms of low-temperature performance, as shown in Fig. 4(f), the initial discharge specific capacity of the Li|CPHL|NCM811 cell was 135.5 mAh·g^{-1} at −10 °C and 0.3 C, and can be stably cycled for 310 cycles. Furthermore, the temperature adaptability of Li||NCM811 full cells was assessed. The cells operated stably within the temperature range of − 20 °C to 80 °C (Fig. 4(g)). Additionally, we assembled Li||NCM811 pouch cell to assess the practical application potential of CPHL electrolyte. The Li|CPHL|NCM811 pouch cell can cycle stably for 50 cycles at a current density of 0.2 C (Fig. S26 in the ESM). Furthermore, the pouch cell can illuminate an LED at different temperatures (0 °C, 25 °C, and 60 °C) (Fig. 4(h)). To further examine the safety of CPHL-based pouch cells, we utilized the infrared camera to detect temperature during the abuse test including initial, folding, needling, and cutting. Despite slight temperature rise, the absence of thermal runaway emphasizes the safety of the CPHL-based cells even under strenuous conditions (Fig. 4(i)). These results indicate that CPHL electrolyte display excellent

Nano Research Energy
ISSN 2791-0091 (print); 2790-8119 (online)
https://doi.org/10.26599/NRE.2026.9120254
Research Article

stability on high-voltage cathodes, highlighting its potential for application in high-energy density solid-state batteries.

2.4 Analysis of cathode-electrolyte interfacial compatibility

High-resolution transmission electron microscopy (HRTEM) was employed to examine the NCM811 cathodes after 50 cycles with the two electrolytes. As shown in Figs. 5(a) and 5(b), the CPHL electrolyte enabled the formation of a uniform and thin cathode electrolyte interface (CEI) layer (~7.8 nm) on the NCM811 particles, and Ni, Co, Mn, O elements were uniformly distributed, demonstrating its superior ability to construct a stable cathode-electrolyte interphase.

These results suggested that SIP-LLZTO facilitated efficient Li^+ transport between the electrolyte and electrode. In striking contrast, a thick and uneven CEI layer (~11.7 nm) was observed on the NCM811 cathode surface using the PHL electrolyte, indicating its insufficient stability under high-voltage operation and the occurrence of severe interfacial side reactions (Fig. 5(c)). The (003)/(104) peak intensity ratio (R) serves as an indicator of the extent of cation mixing (Li^+/Ni^{2+} mixing) in the cathode materials. XRD analysis revealed that the *R* values for PHL and CPHL are 1.23 and 2.23, respectively. The higher *R* value of CPHL reflected low cation mixing, excellent structural ordering, and superior cycling performance. Conversely, the lower R value of PHL indicated severe cation mixing and structural defects in the cycled NCM811 cathode, which block Li^+ diffusion pathways, cause capacity fading, and may induce structural collapse upon cycling (Fig. 5(d)) [45].

Nano Research Energy

ISSN 2791-0091 (print); 2790-8119 (online)

https://doi.org/10.26599/NRE.2026.9120254

Research Article

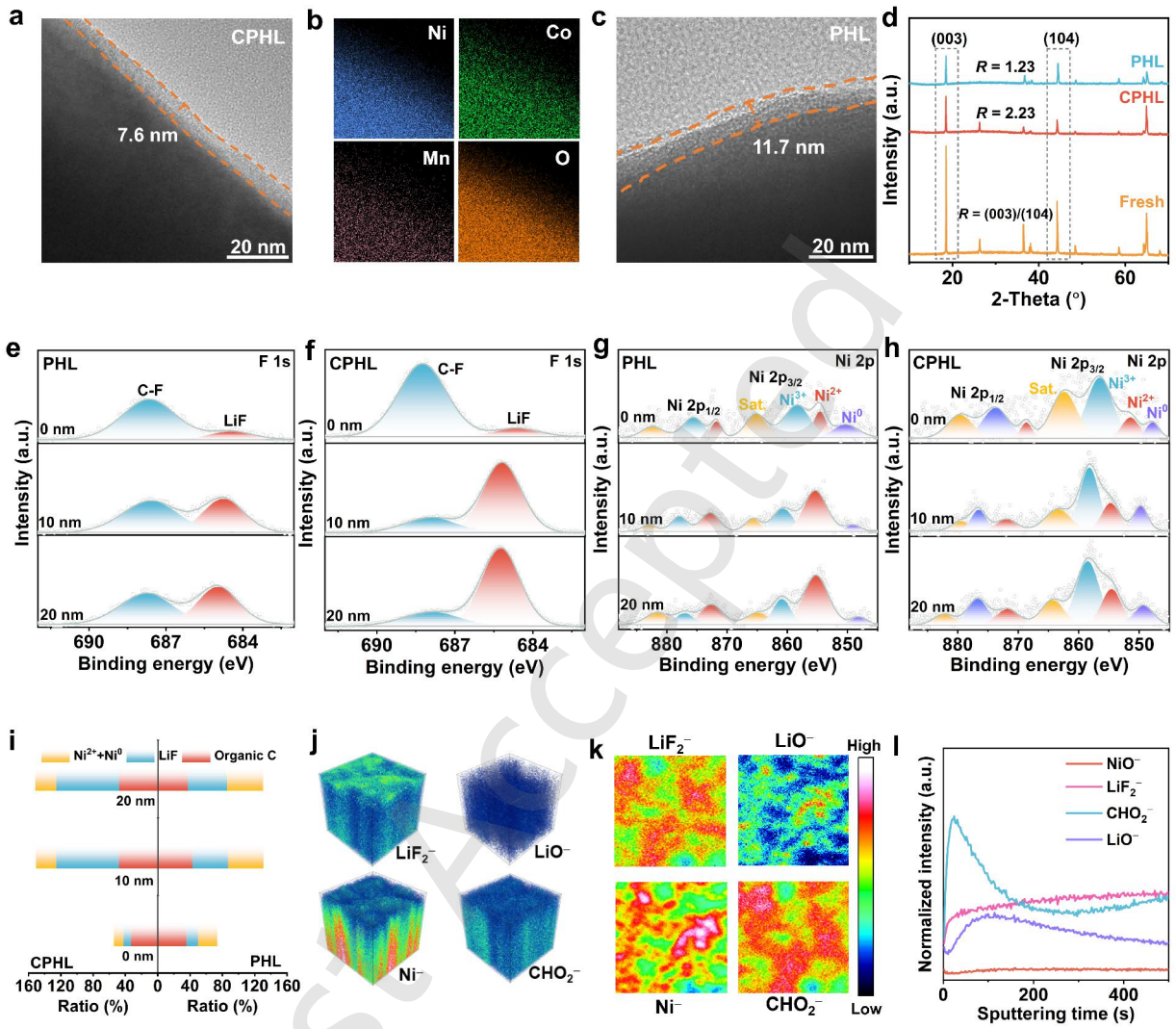

Figure 5 (a) TEM image of cycled NCM811 cathode in CPHL-based cells. (b) EDS mappings of CPHL. (c) TEM image of cycled NCM811 cathode in PHL-based cells. (d) XRD patterns of pristine and cycled NCM811 cathode. (e–h) XPS depth profiles of F 1s and Ni 2p of cycled NCM811 cathodes with PHL and CPHL electrolytes. (i) Comparison of organic C, LiF, and reduced Ni content distribution in the cycled NCM811 cathodes based on PHL and CPHL electrolytes. (j) Corresponding 3D and (k) 2D reconstruction and (l) TOF-SIMS depth profiles of NCM811 cathode with CPHL.

XPS depth profiling was further conducted to investigate the chemical composition of the CEI formed on the NCM811 cathode surface after 50 cycles. Combining C 1s and O 1s, significant differences between the two interfaces were revealed. The CEI layer of PHL was mainly composed of thick organic layers and Li_2CO_3. Due to severe solvent decomposition, its resistivity was high, which explained its poor cycling performance. In

Nano Research Energy
ISSN 2791-0091 (print); 2790-8119 (online)
https://doi.org/10.26599/NRE.2026.9120254
Research Article

contrast, CPHL showed fewer organic decomposition products, owing to the improved interfacial contact enabled by SIP-LLZTO. Furthermore, the CEI derived from the CPHL electrolyte showed a significantly higher LiF content (78.3% at an etching depth of 20 nm). These results demonstrated that the CPHL electrolyte incorporating SIP-LLZTO facilitated the formation of an inorganic-rich CEI, which better preserved the structural integrity of the cathode, which exhibited superior Li^+ transport capability, and effectively enhanced interfacial stability (Figs. 5(e) and 5(f) and Fig. S27 in the ESM) [25, 46]. The Ni 2p spectrum showed that the Ni^{2+}/Ni^{3+} ratio in CPHL was lower than that in PHL, indicating a possible lower degree of Li/Ni mixing, similar to the XRD results of NCM811 positive electrode after cycling (Figs. 5(g) and 5(h)). Compared with PHL, CPHL exhibited a reduced organic C fraction through the depth profile, while LiF became more prominent (Fig. 5(i)). These findings further indicate that the CPHL-derived CEI effectively mitigated electrolyte corrosion at the cathode interface and inhibited Ni dissolution [30, 47]. To gain deeper insight into the chemical composition and spatial distribution of the CEI, time-of-flight secondary ion mass spectrometry (TOF-SIMS) was employed. As depicted in the three-dimensional (3D) reconstructed images and corresponding depth profiles (Figs. 5(j)–5(l)), the CEI derived from the CPHL-containing cell exhibited significant LiF_2^- signal, while the signal for the organic fragments (CHO_2^-) was weak. These results demonstrated that CPHL facilitated the formation of an inorganic-rich CEI while suppressing electrolyte decomposition [48].

3 Conclusion

In summary, we report a solid inorganic plasticizer (SIP) engineering strategy to address the limitations of conventional CPEs in high-voltage lithium metal batteries (HV-LMBs) across a wide-temperature. By modifying the fast Li^+ conductor LLZTO with ionic liquids, we successfully functionalized it as an SIP within the PVDF-HFP matrixes, this observation significantly enhanced composite compatibility and constructing multidimensional Li^+ transport pathways. These advances endow the CPE with a high room-temperature ionic conductivity of 4.72×10^{-4} $S\cdot cm^{-1}$, a Li^+ transference number of 0.59, and nearly doubled mechanical strength and toughness compared to traditional composites. Benefiting from these merits, the Li||Li symmetric cell achieves a high critical current density of 1.8 $mA\cdot cm^{-2}$ and stable cycling over 2100 h. Meanwhile, the Li||NCM811 full cell exhibits exceptional long-term stability, it retains 99.5% of its capacity after 250 cycles at RT, and operates stably for over 400 cycles at 60 °C and 310 cycles at − 10 °C. This work not only demonstrates the effectiveness of surface ionic liquid modification for constructing functional inorganic fillers but also provides a simple and universal strategy for developing high-performance CPEs toward

Nano Research Energy

ISSN 2791-0091 (print); 2790-8119 (online)

https://doi.org/10.26599/NRE.2026.9120254

Research Article

high-energy-density and wide-temperature HV-LMBs.

Declaration of conflicting interests

The authors declare no conflicting interests regarding the content of this article. Prof. Shimou Chen is an Editorial Board Member of *Nano Research Energy*.

Data availability

All data needed to support the conclusions in the paper are presented in the manuscript and/or the Supplementary Materials. Additional data related to this paper may be requested from the corresponding author upon request.

Electronic Supplementary Material: Supplementary material (Please send us a short summary regarding the Supporting info, thanks) is available in the online version of this article at https://doi.org/10.26599/NRE.2026.9120254.

Acknowledgements

S. Chen would like to acknowledge the financial support by the National Natural Science Foundation of China (Nos. 52425207 and 52171198), Beijing Natural Science Foundation (L257027), and the Fundamental Research Funds for the Central Universities (buctrc202104).

References

[1] Ao, X.; Wang, Z.; Zhao, S.; Zhou, J.; Liao, X.; Li, Y.; Zhou, N.; Tian, B.; Wang, H. Crystal facet engineering of BiOCl fillers in solid polymer electrolytes. *Angew. Chem. Int. Ed.* **2025**, 65, e17142.

[2] Ge, W. Preparation of MXene modified by vanadium ion and their application in lithium-sulfur batteries[J]. *J. Xinyang Norm. Univ. (Nat. Sci. Ed.)* **2024**, 37, 147-153.

[3] Chen, J.; He, C.; Peng, X.; Li, J.; Xu, X.; Zhou, Y.; Shen, J.; Sun, J.; Li, Y.; Zhao, T. Puzzle-like molecular assembly of non-flammable solid-state polymer electrolytes for safe and high-voltage lithium metal batteries. *Nat. Commun.* **2025**, 16, 8494.

[4] Zhu, Q.; Yang, K.; Chen, L.; An, X.; Guo, S.; Li, Y.; Ma, Y.; Cao, Y.; Liu, M.; He, Y. B. Activating interfacial ion exchange in composite electrolytes to realize high‐rate and long‐cycling solid‐state lithium batteries. *Angew. Chem. Int. Ed.* **2025**, 64, e202425221.

[5] Chen, L.; Gu, T.; Mi, J.; Li, Y.; Yang, K.; Ma, J.; An, X.; Jiang, Y.; Zhang, D.; Cheng, X.; Guo, S.; Han, Z.; Hou, T.; Cao, Y.; Liu, M.; Lv, W.; He, Y.-B.; Kang, F. Homogeneous polymer-ionic solvate electrolyte with weak dipole-dipole interaction enabling long cycling pouch lithium metal battery. *Nat. Commun.* **2025**, 16.

[6] Bai, C.; Li, Y.; Xiao, G.; Chen, J.; Tan, S.; Shi, P.; Hou, T.; Liu, M.; He, Y.-B.; Kang, F. Understanding the electrochemical window of solid-state electrolyte in full battery application. *Chem. Rev.* **2025**, 125, 6541-6608.

[7] Chen, Y.; Jing, L.; Cai, W.; Cao, Z.; Ma, C.; Li, R.; Wu, Y.; Lv, S.; Zhai, Y.; Yang, W.; Wang, Y.; Fu, X. A gradient nanodomain high‐entropy polymer electrolyte tape forpressure‐free solid‐state lithium batteries. *Adv. Mater.* **2026**, 38, e20657.

[8] Cao, K.; He, Y.; Wang, S.; Fu, J.; Liu, H. Construction and K-ion storage properties of SnS_2/SnS/NC heterostructures micro-flowers[J]. *J. Xinyang Norm. Univ. (Nat. Sci. Ed.)* **2024**, 37, 141-146.

[9] Zhao, Y.; Ma, Y.; Yang, J.; Chen, L.; Guo, S.; Jiang, C.; Li, Y.; An, X.; Shang, G.; Li, B.; Fu, Z.; Cheng, X.; Hou, T.; He, Y. B. Electron percolating shielded interlayer enabling ultra-stable all‐solid‐state lithium metal batteries. *Adv. Mater.* **2025**, 38, e15687.

Nano Research Energy

ISSN 2791-0091 (print); 2790-8119 (online)

https://doi.org/10.26599/NRE.2026.9120254

Research Article

[10] Du, L.; Xu, L.; Yao, M.; Tang, C.; Xiao, Y.; Ding, C.; Zhao, M.; Hu, A.; Zhang, Y.; Lu, J. Combined ion‐expressway and Li^+‐transit lane in asymmetric polymer electrolyte enables high‐voltage solid‐state lithium‐metal‐batteries. *Adv. Energy Mater.* **2025**, 16, e05169.

[11] Zhang, C.; Zhao, L.; Li, F.; Song, X.; Chen, J.; Zeng, J.; Xi, L.; Hu, R.; Zhu, M.; Liu, J. Optimizing the electron density of PVDF‐HFP‐based solid polymer electrolyte by donor–acceptor COF toward high‐performance solid‐state lithium metal batteries. *Adv. Mater.* **2025**, 37, e13427.

[12] Zhao, Y.; Shi, J.; Yang, H.; Geng, C.; Hu, Z.; Zhang, B.; Sun, Z.; Wang, M.; Jiang, C.; Lan, J.; Chen, W.; Lv, W.; Yang, Q.-H. Catalyzing Li-salt dissociation and decomposition for a conformal low-impedance solid electrolyte interphase in solid-state Li metal batteries. *J. Am. Chem. Soc.* **2026**, 148, 11540-11550.

[13] Fan, Y.; Zhu, M.; Wang, H.; Hong, Z.; Zhao, B.; Ke, H.; Jiang, Y.; Zhu, M.; Chen, P.; Liu, Z.; Bai, Z.; Ge, M.; Feng, Y.; Chen, S.; Shao, H.; Malyi, O. I.; Tang, Y. Polyamine‐mediated proton/$TFSI^-$ dual capture enables high‐voltage PEO‐based all‐solid‐state Li batteries. *Adv. Mater.* **2026**, 38, e20538.

[14] He, C.; Ying, H.; Cai, L.; Chen, H.; Xu, Z.; Liu, S.; Huang, P.; Zhang, H.; Song, W.; Zhang, J.; Shi, L.; Gao, W.; Li, D.; Han, W. Q. Tailoring stable PEO‐based electrolyte/electrodes interfaces via molecular coordination regulating enables 4.5 V solid‐state lithium metal batteries. *Adv. Funct. Mater.* **2024**, 34, 2410350.

[15] Long, S.; Gui, B.; Li, C.; Yang, B.; Sun, L.; Zhan, Y.; Huang, C.; Tian, J.; Wu, F.; Chen, N.; Chen, R. Deep eutectic interlayer design for stability enhancement in LLZTO solid‐state lithium batteries. *Adv. Funct. Mater.* **2025**, 36, e13024.

[16] Zhang, D.; Liu, Y.; Li, D.; Li, S.; Xiong, Q.; Huang, Z.; Wang, S.; Hong, H.; Zhu, J.; Lv, H.; Zhi, C. Salt dissociation and localized high-concentration solvation at the interface of a fluorinated gel and polymer solid electrolyte. *Energy Environ. Sci.* **2025**, 18, 227-235.

[17] Huang, Z.; Wang, Z.; Chen, X.; Yang, L.; Huang, T.; He, X.; Huang, W.; Chen, J.; Yang, X.; Chen, L.; Liao, B.; Ouyang, X.; Liu, J.; Ren, X.; Pan, F.; Zhang, Q.; Hu, J. Interface engineering and optimization strategies for high‐energy‐density batteries based on polymer composite electrolytes. *Adv. Mater.* **2025**, e04186.

[18] Zhou, X.; Cai, R.; Chen, Q.; Zhang, Q.; Rena, R.; Shen, Y.; Liang, Y.; Chen, J.; Zhu, H.; Duan, H. Constructing ion bridges with competitive coordination effects to promote Li^+ conduction in solid‐state electrolytes for high‐performance lithium metal batteries. *Adv. Mater.* **2026**, 38, e23369.

[19] Nie, Y.; Luo, D.; Yang, T.; Wang, X.; Li, S.; Feng, G.; He, L.; Shao, Y.; Wang, J.; Jin, M.; Wang, X.; Chen, Z. Ultrathin electrolyte membranes with reinforced concrete structure for fast‐charging solid‐state lithium metal batteries. *Adv. Mater.* **2025**, 37, 2504092.

[20] Zhang, J.; Li, S.; Wang, X.; Mao, S.; Guo, J.; Shen, Z.; Mao, J.; Wu, Q.; Shen, K.; Cheng, H.; Tan, Y.; Lu, Y. Construction of stable Li_2O‐rich solid electrolyte interphase for practical PEO‐based Li‐metal batteries. *Adv. Energy Mater.* **2023**, 2302587.

[21] Liu, F.; Gao, L.; Du, Y.; Duan, J.; Li, H.; Wang, M.; Li, F.; Yu, R.; Zhang, C.; Liu, S. Preparation of PEDOT: PSS/Fe_3O_4 composite films and their supercapacitor properties[J]. *J. Xinyang Norm. Univ. (Nat. Sci. Ed.)* **2024**, 37, 24-29.

[22] Xu, Y.; Wang, K.; Zhang, X.; Ma, Y.; Peng, Q.; Gong, Y.; Yi, S.; Guo, H.; Zhang, X.; Sun, X.; Gao, H.; Xin, S.; Guo, Y. G.; Ma, Y. Improved Li‐ion conduction and

Nano Research Energy

ISSN 2791-0091 (print); 2790-8119 (online)

https://doi.org/10.26599/NRE.2026.9120254

Research Article

(electro)chemical stability at garnet‐polymer interface through metal‐nitrogen bonding. *Adv. Energy Mater.* **2023**, 13, 2204377.

[23] Wang, H.; Wen, P.; Liu, Y.; Han, S.; Zhang, Z.; Xu, Y.; Chen, M.; Lin, X. Single-ion polymer-in-salt electrolytes enabling percolating ionic nanoaggregates for ambient-temperature solid-state batteries. *J. Am. Chem. Soc.* **2025**, 147, 14554-14563.

[24] Lu, D.; Li, R.; Rahman, M. M.; Yu, P.; Lv, L.; Yang, S.; Huang, Y.; Sun, C.; Zhang, S.; Zhang, H.; Zhang, J.; Xiao, X.; Deng, T.; Fan, L.; Chen, L.; Wang, J.; Hu, E.; Wang, C.; Fan, X. Ligand-channel-enabled ultrafast Li-ion conduction. *Nature* 2024, 627.

[25] Tao, F.; Yan, K.; Dong, C.; Wang, J.; Pan, Q.; Gong, M.; Gu, J.; Shen, C.; Yu, R.; Jiang, Y.; Yuan, M.; Zhou, C.; Huang, M.; Xu, X.; Mai, L. Electric‐dipole coupling ion‐dipole engineering induced rational solvation‐desolvation behavior for constructing stable solid‐state lithium metal batteries. *Angew. Chem. Int. Ed.* **2025**, 64, e202503037.

[26] Sun, W.; Yu, Q.; Tian, H.; Qiu, Q.; Qiu, S.; Gomez, J. F. F.; Ullah, I.; Huang, L.; Wu, X.; Xia, L.; Ai, X. Asymmetrically fluorinated alkoxysilane single‐solvent electrolytes enable high‐voltage and long‐cycling lithium metal batteries. *Angew. Chem. Int. Ed.* **2025**, 65, e17203.

[27] Qiu, B.; Wen, J.; Xu, F.; Zhao, R.; He, C.; Zhang, P.; Lin, Z.; Mi, H. Unveiling the dilution‐shielding effect as a universal strategy for interfacial regulation in composite polymer electrolytes. *Angew. Chem. Int. Ed.* **2026**, 65, e8139928.

[28] Zhang, D.; Liu, Y.; Li, D.; Li, S.; Xiong, Q.; Huang, Z.; Wang, S.; Hong, H.; Zhu, J.; Zhi, C. Modulating salt dissociation and solvent immobilization through dipole interactions in polymer electrolytes for lithium metal batteries. *Adv. Mater.* **2025**, 38, e12960.

[29] Ma, X.; Yu, J.; Gui, X.; Liu, Y.; Hu, Y.; Pan, L.; She, Y.; Kuang, Y.; Cheng, T.; Yan, F. Dual-ion confined-region channels enable rapid ion transport for all-solid-state lithium metal batteries. *J. Am. Chem. Soc.* **2026**, 148, 8784-8794.

[30] Xiao, T.; Xian, J.; Yu, Z.; Zhi, Z.; Zheng, J.; Yan, W.; Liu, K.; Yang, P. Cationic-zwitterionic polymer electrolytes with enhanced ionic conductivity and lithium‐ion selectivity for solid‐state batteries. *Angew. Chem. Int. Ed.* 2025, 64, e202514027.

[31] Chen, Y.; Yang, X.; Wang, T.; Tang, X.; Li, D.; Wang, S.; Lei, Y.; Han, Y.; Chen, S.; Armand, M.; Aurbach, D.; Wang, G. Fluoroether design enables high‐voltage all‐solid‐state lithium metal batteries. *Adv. Mater.* **2025**, 37, 2506020.

[32] Lv, Q.; Li, L. a.; Zhang, X.; Wang, R.; Wen, N.; Xue, L.; Wang, H.; Shen, L.; Chen, D.; Ciucci, F.; Wang, J. Developing dynamic ion transport channels in polymer solid electrolytes for high-performance lithium metal batteries. *J. Am. Chem. Soc.* **2025**, 147, 27611-27623.

[33] Zhu, J.; Bian, P.; Sun, G.; Zhang, J.; Lou, G.; Song, X.; Zhao, R.; Liu, J.; Xu, N.; Li, A.; Wan, X.; Ma, Y.; Li, C.; Zhang, H.; Chen, Y. Practical high‐voltage lithium metal batteries enabled by the in‐situ fabrication of main‐chain fluorinated polymer electrolytes. *Angew. Chem. Int. Ed.* **2025**, 64, e202424685.

[34] Wang, L.; Xie, L.; Ma, J.; Liu, Y.; Deng, N.; Wang, Z.; Li, L.; Gao, S. "Ionic tug‐of‐war" effect decoupling Li^+‐coordination enables high ion conductivity and interface stability for solid‐state electrolytes. *Adv. Energy Mater.* **2026**, 65, e05982.

[35] Ma, X.; Yu, J.; Zou, X.; Hu, Y.; Yang, M.; Zhang, F.; Yan, F. Single additive to regulate lithium-ion solvation structure in carbonate

Nano Research Energy

ISSN 2791-0091 (print); 2790-8119 (online)

https://doi.org/10.26599/NRE.2026.9120254

Research Article

electrolytes for high-performance lithium-metal batteries. *Cell Rep. Phys. Sci.* **2023**, 4, 101379.

[36] Hao, Z.; Chen, Y.; Peng, Q.; He, L.; Han, Y.; Gong, J.; Shen, Z.; Zhao, S.; Wang, G.; Chen, S. Harnessing spatiotemporal dynamics of polymerized electrolytes for durable high-voltage lithium metal batteries. *J. Am. Chem. Soc.* **2026**, 148, 11726−11737.

[37] Gou, J.; Cui, K.; Wang, S.; Zhang, Z.; Huang, J.; Wang, H. An anisotropic strategy for developing polymer electrolytes endowing lithium metal batteries with electrochemo-mechanically stable interface. *Nat. Commun.* **2025**, 16, 3626.

[38] Yang, B.; Deng, C.; Chen, N.; Zhang, F.; Hu, K.; Gui, B.; Zhao, L.; Wu, F.; Chen, R. Super‐ionic conductor soft filler promotes Li^+ transport in integrated cathode-electrolyte for solid‐state battery at room temperature. *Adv. Mater.* **2024**, 36, 2403078.

[39] Gong, J.; Peng, Q.; Zhao, S.; Wen, T.; Xu, H.; Ma, W.; Yao, Z.; Chen, Y.; Wang, G.; Chen, S. Built-in single-ion-conducting polymer bridges for superior ion transport enabling long-life and high-voltage lithium–metal batteries. *Energy Environ. Sci.* **2025**, 18, 5511-5523.

[40] Zhu, J.; He, S.; Tian, H.; Hu, Y.; Xin, C.; Xie, X.; Zhang, L.; Gao, J.; Hao, S. M.; Zhou, W.; Zhang, L. The influences of DMF content in composite polymer electrolytes on Li^+‐conductivity and interfacial stability with Li‐Metal. *Adv. Funct. Mater.* **2023**, 33, 2301165.

[41] Jin, L.; Chen, J.; Xu, X.; Wang, Z.; Guo, Z.; Lin, P.; Sun, J.; Huang, B.; Zhao, T. Electrolyte/electrode interphase regulation with methylthiolation ionic liquids for high-voltage quasi-solid-state Li metal batteries. *Sci. Adv.* **2025**, 11, eadz5203.

[42] Lan, J.; Zhong, Y.; Peng, H.; Meng, Z. D.; He, N. X.; Lan, S. Z.; Huang, L.; Sun, S. G.; Deng, Y.-P. Constructing an anion-capturing interface to achieve Li^+ cross-phase transport in composite solid electrolytes. *Nat. Commun.* **2025**, 17, 376.

[43] Qin, Y.; Wang, H.; Zhou, J.; Li, R.; Jiang, C.; Wan, Y.; Wang, X.; Chen, Z.; Wang, X.; Liu, Y.; Guo, B.; Wang, D. Binding FSI^- to construct a self-healing SEI film for Li-metal batteries by in-situ crosslinking vinyl ionic liquid. *Angew. Chem. Int. Ed.* **2024**, e202402456.

[44] Liu, C.; Jia, S.; Yang, T.; Liu, J.; Zhou, X.; Wang, Z.; Dong, H.; Shi, Z.; Zhang, Y.; Chen, Z. Scalable and ultrathin dual entangled network polymer electrolytes for safe solid‐state sodium batteries. *Angew. Chem. Int. Ed.* **2025**, 64, e202505938.

[45] Sun, Z.; Yang, J.; Wu, Y.; Meng, F.; Niu, Y.; Xu, H.; Zhu, Y.; Hong, B.; Chen, Z.; Zhu, J.; He, Q.; Wu, G.; Chen, W. Stabilizing residual monomers within in situ polymerized electrolytes for high-voltage lithium metal batteries. *J. Am. Chem. Soc.* **2025**, 147, 18064-18073.

[46] Xiao, G.; Yang, K.; Qiu, Y.; Shi, P.; Zhong, G.; An, X.; Ma, Y.; Chen, L.; Guo, S.; Mi, J.; Han, Z.; Hou, T.; Yan, H.; Tian, Y.; Zhang, X.; Cao, Y.; Liu, M.; Zhou, Z.; He, Y. B. Dielectric‐tailored space charge layer and ion coordination structure for high‐voltage polymer all‐solid‐state lithium batteries. *Adv. Mater.* **2025**, 37, 2415411.

[47] Duan, S.; Lu, Z.; Zheng, Y.; Liu, X.; Zhang, L.; Li, Z.; Liu, Z.; Luo, Y.; Qin, B.; Liu, Y.; Pei, M.; Xu, J.; Lin, X.; Yan, W.; Zhang, J. Directionally aligned “mechanical balance” design enables near-frictionless Li^+ transport in polymer electrolytes. *J. Am. Chem. Soc.* **2025**, 148, 2972-2984.

[48] Yin, X.; Guo, Y.; Chi, S.; Jia, Y.; Li, F.; Qi, J.; Yi, X.; Wu, S.; Yang, Q. H. Beyond polymerization: In situ coupled fluorination enables more stable interfaces for solid-state

Nano Research Energy

ISSN 2791-0091 (print); 2790-8119 (online)

https://doi.org/10.26599/NRE.2026.9120254

Research Article

lithium batteries. *J. Am. Chem. Soc.* **2025**, 147, 4393-4402.

Nano Research Energy

ISSN 2791-0091 (print); 2790-8119 (online)

https://doi.org/10.26599/NRE.2026.9120254

Research Article

Author biography

Qimin Peng is a Ph.D. candidate in Materials Science and Engineering at Beijing University of Chemical Technology, under the supervision of Prof. Shimou Chen. Her research focuses on the development of solid-state batteries and related functional materials. She has published more than five first-author papers in journals such as Journal of Energy Chemistry, Applied Catalysis B: Environmental and Energy, Nano Energy, Journal of Colloid and Interface Science, and ChemSusChem.

Yong Chen is a Ph.D. candidate at the Centre for Clean Energy Technology, Faculty of Science, University of Technology Sydney. His research focuses on solid-state batteries and related energy materials. He has published over 20 first-author or corresponding-author papers in high-impact SCI-indexed journals, including Energy Storage Materials, Advanced Functional Materials, Advanced Materials, Angewandte Chemie International Edition, Advanced Science, Energy & Environmental Science, Nature Communications, and Journal of the American Chemical Society.

Shimou Chen is a professor and Ph.D. supervisor at Beijing University of Chemical Technology, a recipient of the National Science Fund for Distinguished Young Scholars, and a Fellow of the Royal Society of Chemistry. His research interests include key materials and integrated device design for lithium-ion batteries, solid-state batteries, and zinc-ion batteries. He has published over 180 SCI-indexed papers in prestigious journals such as Journal of the American Chemical Society, Angewandte Chemie International Edition, Advanced Materials, and Nature Communications, and holds more than 40 granted Chinese invention patents.

Electronic Supplemental Materials

Solid-state ion plasticizer-engineered composite polymer electrolytes for high-voltage and wide-temperature lithium metal batteries

Qimin Peng[1], Yong Chen[2] (✉), Jiajun Gong[1], Zhiye Hao[1], Guoxiu Wang[2], and Shimou Chen[1] (✉)

[1]State Key Laboratory of Chemical Resource Engineering, Beijing Key Laboratory of Electrochemical Process and Technology of Materials, Beijing University of Chemical Technology, Beijing 100029, China

[2]Centre for Clean Energy Technology, University of Technology Sydney, Broadway, Sydney, NSW 2007, Australia

Supporting infomation to https://doi.org/10.26599/NRE.2026.9120254

Address correspondence to Yong Chen, yong.chen@student.uts.edu.au; Shimou Chen, chensm@buct.edu.cn

1 Experimental sections

1.1 Materials

Poly(vinylidene fluoride-co-hexafluoropropylene) (PVDF-HFP, Mw=400,000) was purchased from Dongguan Hongfu Plastics Trading Department. $Li_{6.4}La_3Zr_{1.4}Ta_{0.6}O_2$ (LLZTO) (500 nm) was purchased from Shenzhen Kejing Star Technology company. 1-carboxyethyl-3-methylimidazolium trifluoromethanesulfonate (HOOCEMImOTf) was purchased from Qingdao Aoliko New Material Technology Co., Ltd. N, N-dimethylformamide (DMF), 1-Methyl-2-pyrrolidinone (NMP), and ethanol were purchased from Shanghai Aladdin Biochemical Technology Co., Ltd. Lithium bis(trifluoromethane)sulfonimide (LiTFSI), propylene carbonate (PC), succinonitrile (SN), Lithium nitrate ($LiNO_3$) were purchased from Shanghai Songjing New Energy Technology Co.,Ltd. Commercial cathode materials $LiFePO_4$ (LFP), $LiNi_{0.8}Co_{0.1}Mn_{0.1}O_2$ (NCM811), PVDF 5130 (Mw=1200 000), Super P (SP), Li foils (450 μm), and Li coated Cu foil (50 μm Li) were purchased from Guangdong Canrd New Energy Technology Co., Ltd.

1.2 Synthesis of composite solid electrolyte

1.2.1 Preparation of SIP-LLZTO

Firstly, HOOCEMImOTf was added to an anhydrous ethanol solution and dissolved in it to form 0.1 M solution. LLZTO ceramic particles with the same mass of HOOCEMImOTf were then added and the mixture was stirred for 24 h. The suspension was centrifuged, and then precipitate was washed three times in ethanol, and dried at 60 °C to obtain the SIP-LLZTO. The main surface reactions can be expressed as follows:

$HOOCEMImOTf + LiOH \rightarrow [LiOOCEMIm][OTf] + H_2O$

$HOOCEMImOTf + Li_2CO_3 \rightarrow [LiOOCEMIm][OTf] + CO_2 + H_2O$

1.2.2 Preparation of CPHL electrolytes

Briefly, 0.4 g PVDF-HFP, 0.08 g SIP-LLZTO, and 0.3 g LiTFSI were dissolved in DMF solvent. The mixture was stirred at RT for 12 h to obtain a homogeneous slurry, which was then dried at 60 °C for 24 h to obtain CPHL electrolyte by the solution casting method. For comparison, 0.08 g LLZTO was added to the mixed solution of PVDF-HFP/LiTFSI electrolyte to obtain PHL electrolyte.

1.3 Material characterizations

The crystalline phases of the powder and membrane were analyzed using X-ray diffraction (XRD), with a scanning range of 10-90° and a scanning rate of 10° min^{-1}. The Fourier Transform Infrared (FT-IR) spectroscopy measurement of the membranes were conducted on SHIMADZU-IRTracer-100 in attenuated total reflection (ATR) mode. In-situ FTIR experiment was performed with a Thermo Fisher Scientific Nicolet iS50 spectrometer FT-IR instrument and a single-reflection diamond attenuated total reflection sample cell. Thermogravimetric analysis (TGA) was conducted using a TGA5500 with temperature range of 40-600 °C and a heating rate of 10 °C min^{-1} in nitrogen atmosphere. Raman spectroscopy was recorded using LabRAM Aramis with laser excitation at 785 nm. Solid-state ^7Li NMR was conducted by a Bruker 400WB AVANCE Ⅲ instrument. Sigma 300 field emission scanning electron microscope (SEM) instrument to examine the surface morphology of the samples (MAIA3 XMU), and the elemental distribution were analyzed by energy dispersive spectrometer (EDS). Time-of-flight secondary ion mass spectrometry (TOF-SIMS, IONTOF M6, Bi_3^+, 30 keV) was conducted to identify the CEI compoents within a 50 μm × 50 μm region. The TEM images of cycled NCM811 cathodes were characterized by transmission electron microscope (JEOL-JEM-F200). X-ray photoelectron spectroscopy (XPS)

spectra were recorded from the Thermo Fisher-K-Alpha with a monochromatized micro-focused Al K α X-ray source provided by eceshi (www.wceshi.com). The Young′s modulus and surface roughness of membranes was measured by atomic force microscope (AFM, ASTSCAN2-SYS). Small-angle X-ray scattering (SAXS) measurements were performed by Xenocs Xeuss 2.0.

1.4 Cell assembly and testing

The assembly of CR2025-type coin cells were conducted in an argon-filled glove box with H_2O and O_2 content <0.1 ppm. The cathode slurry for $LiFePO_4$ (LFP, 1 C=170 mAh g^{-1}) and $Ni_{0.8}Co_{0.1}Mn_{0.1}O_2$ (NCM811, 1 C=200 mAh g^{-1}) was synthesized by combining LFP or NCM811, PVDF5130 binder, super P, in a NMP solution with a weight ratio of 8:1:1. Afterwards, the above slurry was coated to Al foil with a doctor blade, and dried at 80 °C for 24 h in a vacuum oven. And the obtained Al foil was cut into 10 mm diameter by a manual cutting machine (MSK-110, Shenzhen Kejing star technology company). Moreover, the average loading mass of obtained LFP and NCM811 cathodes was approximately 2.0 mg cm^{-2}. The coin cells were made with LFP/NCM811 cathode and Li metal anode, and 2.5 μL liquid electrolyte (LiTFSI: PC:SN=1:3:3, wt.%, 0.5wt.% $LiNO_3$) was dropped on the interface between the CSEs and cathodes to ensure sufficient electrodes' wetting. The Li||NCM811 pouch cell was assembled by NCM811, CPHL and 50 μm Li in copper foil. The areas of the NCM811 cathode was 3×4 cm^2. Galvanostatic charging and discharging tests of assembled cells were evaluated by the NEWARE CT-4008T battery testing system.

1.5 Electrochemical characterization

The ionic conductivity (σ) at various temperature of the electrolytes was evaluated through electrochemical impedance spectroscopy (EIS) measurements by Metrohm Auto lab M204 electrochemical workstation (Nova 2.1) in stainless steel (SS) symmetric cells, employing the following equation:

$$\sigma = L/RS \qquad (1)$$

where the L, R and S represent for the thickness, the bulk resistance and the effective contact area of the electrolytes, respectively. To calculate the activation energy (E_a) of the electrolytes, the logarithms of conductivity and temperature were plotted according to the Arrhenius equation.

$$\sigma(T) = Aexp\frac{-E_a}{RT} \qquad (2)$$

where σ (T) stands for the ionic conductivity of electrolytes between 25-70 ° C, and the pre-exponential factor, the thermodynamic constant, and the test temperature (K) are defined by A, R, and T, respectively.

The oxidative stability of electrolytes was researched by testing the linear sweep voltammetry (LSV) curves of SS | | Li cells between 2-6 V with the scan rate of 0.1 mV s^{-1}. The Li^+ transference number (t_{Li^+}) of electrolytes was measured by Li||Li symmetric cells by the electric potential step method under a polarization time of 2000 s. It was calculated using the following equation:

$$t_{Li^+}=\frac{I_S(\Delta V-I_0R_0)}{I_0(\Delta V-I_SR_S)} \qquad (3)$$

where I_0 and I_s represent the currents before and after polarization, ΔV is the applied voltage of 5 mV, R_0 and R_s are the interface resistances of Li||Li symmetric cells before and after polarization.

1.6 Finite element modeling (FEM) simulations

The diffusion and migration of lithium ions in the electrolyte are described using the "Nernst Planck" equation (with corresponding module integration in COMSOL) [S1]. The model geometry (electrolyte region) is 12 um × 12 um, and a triangular region with a side length of 1um and a height of 1um is opened at the bottom and rounded transition is set.

$$N_i = -D_i\nabla c_i - z_i u_{m_i} F c_i \nabla \emptyset_i + c_i u \qquad (1)$$

in which, N_i is the flux, D_i is the diffusion coefficient, c_i is the concentration, z_i is the charge number of the ion, u_{m_i} is the ionic mobility, F is the Faraday constant, $\emptyset_i$ is the electric potential, u is the fluid velocity vector.

To simulate the true ion transfer state inside the battery, the left and right boundaries of the model are set as flux-free boundaries, and a current density of 4 mA cm^{-2} is applied to the top. The initial Li^+ ion concentration of the electrolyte in the model area is 1000 mol m^{-3}. The bottom is set as the lithium negative electrode boundary, and the Butler-Volmer equation is used to describe the charge transfer process on the lithium metal surface. The Butler-Volmer equation describes the kinetics of charge transfer reactions occurring at the electrode-electrolyte interface. It quantifies the dependence of the electrode reaction rate on factors such as overpotential and the concentration of reactants.

$$i_{loc} = i_0 - (\exp\left(\frac{\alpha_a F\eta}{RT}\right) - \exp\left(\frac{-\alpha_c F\eta}{RT}\right)) \quad (2)$$

in which, i_{loc} is the local current density, i_0 is the exchange current density, α_a and α_c are the anodic and cathodic charge transfer coefficients, respectively, F is the Faraday constant, R is the universal gas constant, T is the temperature, η is the overpotential.

1.7 Computational methods

1. Dissociation energy of $LiNO_3$

   $LiNO_3 = Li^+ + NO_3^-$ ΔG=160.6 kcal/mol

2. Dissociation energy of HOOCEMImOTf

   HOOCEMImOTf =$HOOCEMIm^+ + OTf^-$ ΔG=76.8 kcal/mol

3. Dissociation energy of HOOCEMImOTf

   $LiNO_3$ + HOOCEMImOTf = $HOOCEMImNO_3$ + LiOTf ΔG=4.19 kcal/mol

All the calculations were performed with Gaussian09 package. Geometry optimization of all the minima and transition states involved was carried out at the B3LYP[S2, S3] level with the 6-311G(d, p) basis set for C, H, O, N, Li, and S. Default convergence criteria were used. The vibrational frequency calculations were conducted at the same level of theory as geometry optimization to confirm whether each optimized structure is an energy minimum point.

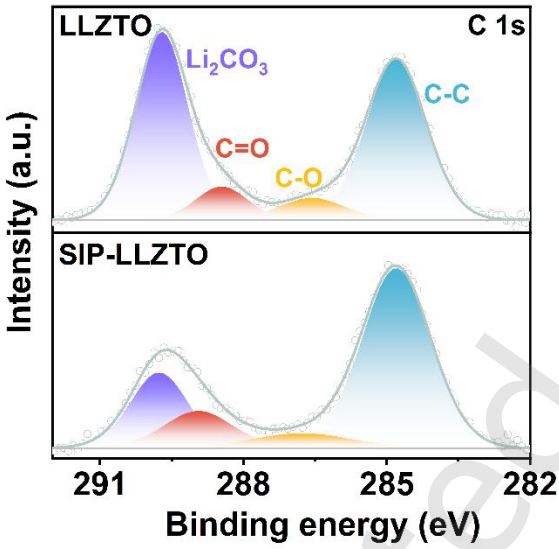

Figure S1 XPS spectra of C 1s of LLZTO and SIP-LLZTO.

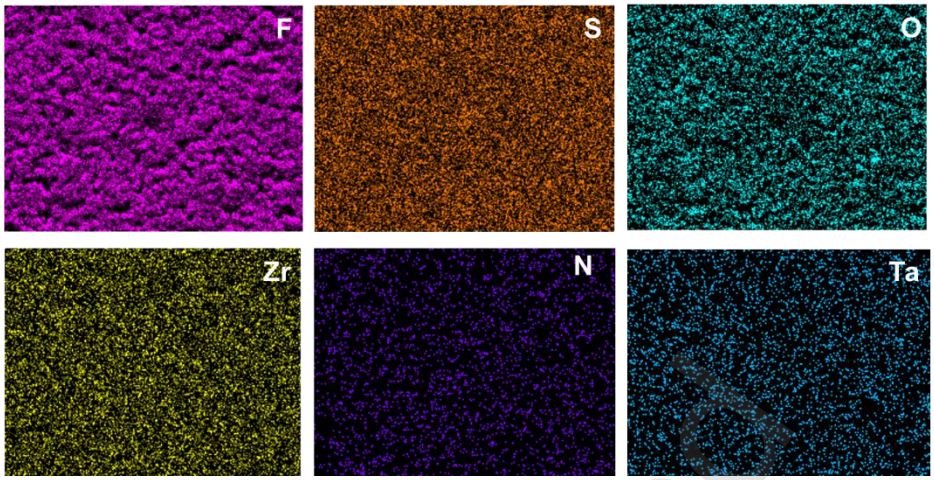

Figure S2 EDS maps of CPHL electrolytes.

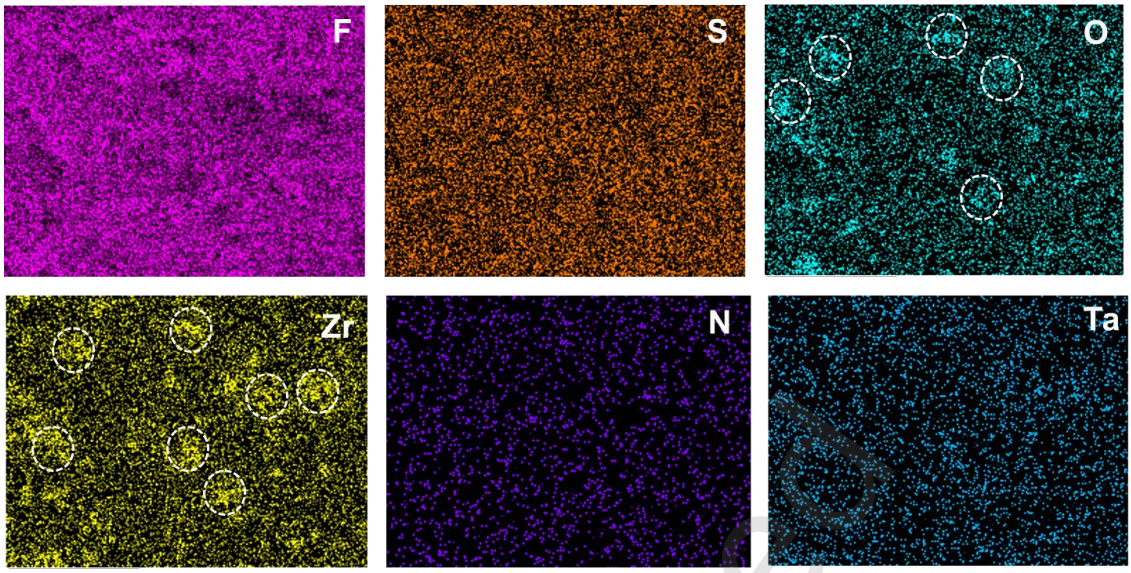

Figure S3 EDS maps of PHL electrolytes.

Note: The alkaline impurities on the LLZTO surface trigger the dehydrofluorination of PVDF-HFP, and the in-situ generated HF etches the surface of LLZTO particles, impairing their dispersion stability. Meanwhile, dehydrofluorination introduces conjugated structures and polar defects along the polymer chains, which strengthen intermolecular interactions and promote strong interfacial adsorption between the polymer and LLZTO. These combined effects eventually cause ceramic particles to agglomerate with each other, forming distinct particle clusters.

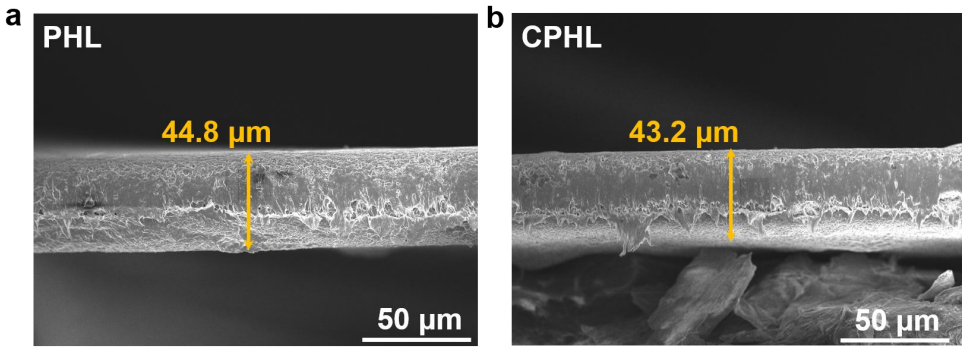

Figure S4 SEM cross-sectional images of (a) PHL and (b) CPHL membrane thickness.

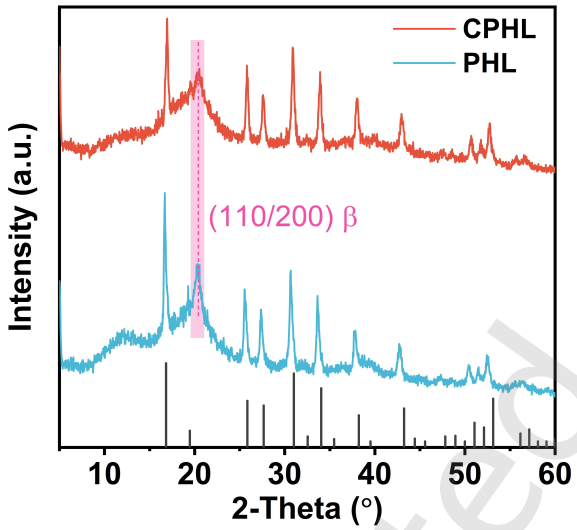

Figure S5 XRD patterns of CPHL and PHL electrolytes.

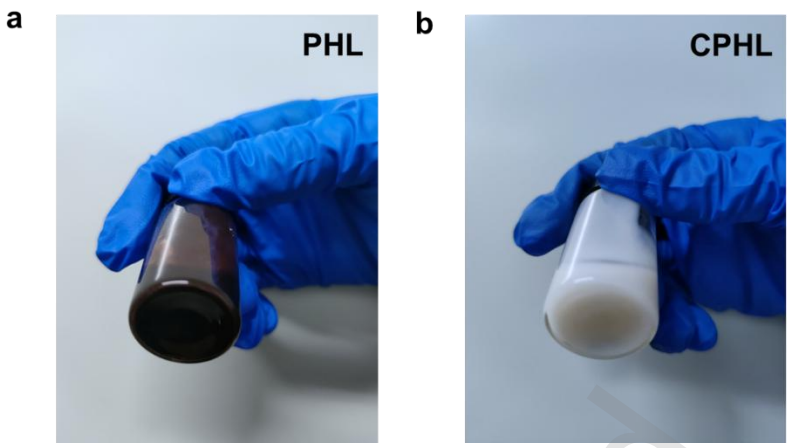

Figure S6 Polymer solutions of (**a**) PHL and (**b**) CPHL.

Note: The alkaline Li_2CO_3 impurities on the surface of LLZTO catalyze the dehydrofluorination of PVDF-HFP. This reaction produces successive carbon-carbon double bonds along the polymer backbone, forming chromophores with a conjugated system. Consequently, the solution turns dark brown. The dehydrofluorinated products remain soluble in DMF, so no obvious precipitate forms at the bottom.

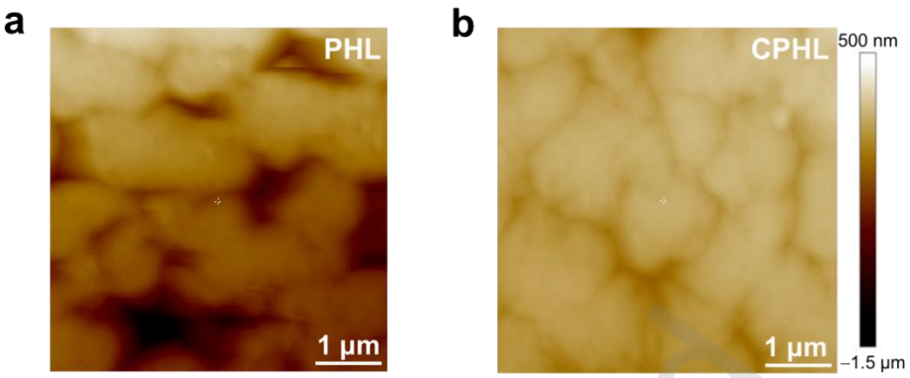

Figure S7 Surface roughness of (**a**) PHL and (**b**) CPHL membrane.

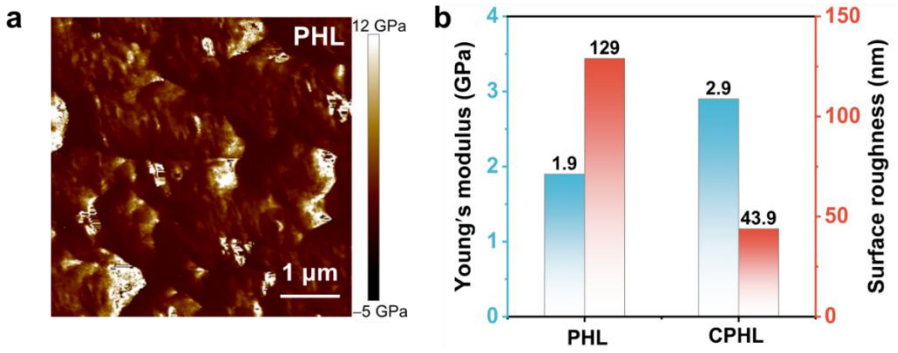

Figure S8 (**a**) Young's modulus of PHL membrane. (**b**) Comparisons of Young's modulus and surface roughness between PHL and CPHL.

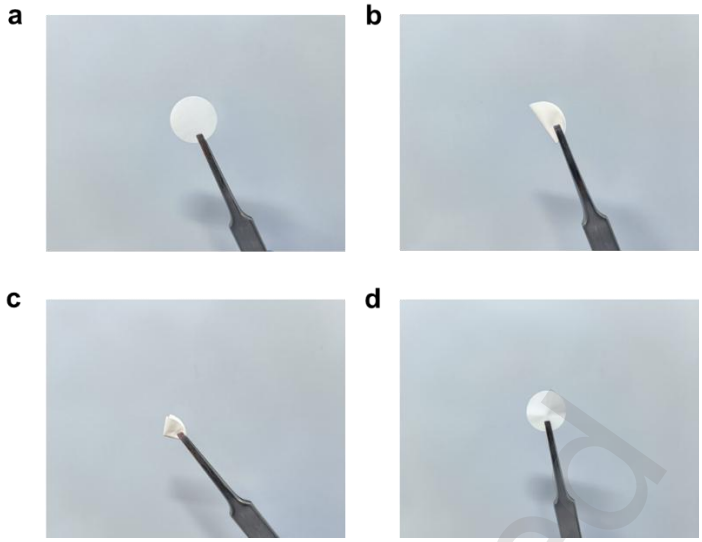

Figure S9 Photographs of CPHL electrolytes with different folded shapes. (**a**) Flattern, (**b**) fold, (**c**) bifold, (**d**) flatten.

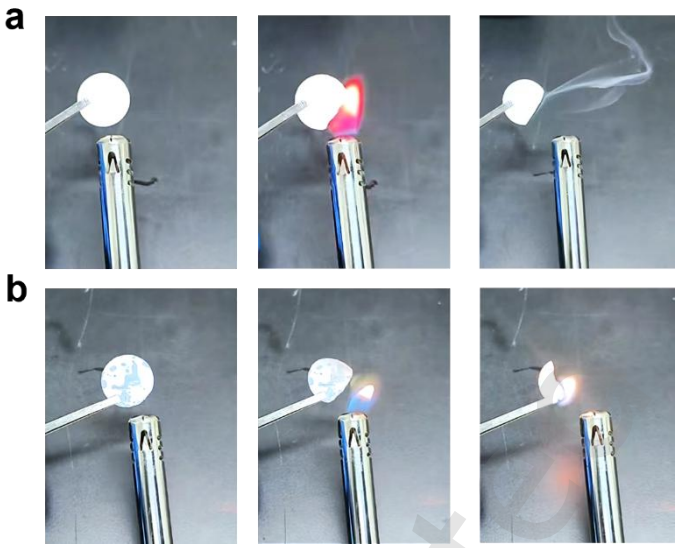

Figure S10 Combustion tests of (a) CPHL electrolyte and (b) Celgard separator immersed with LEs.

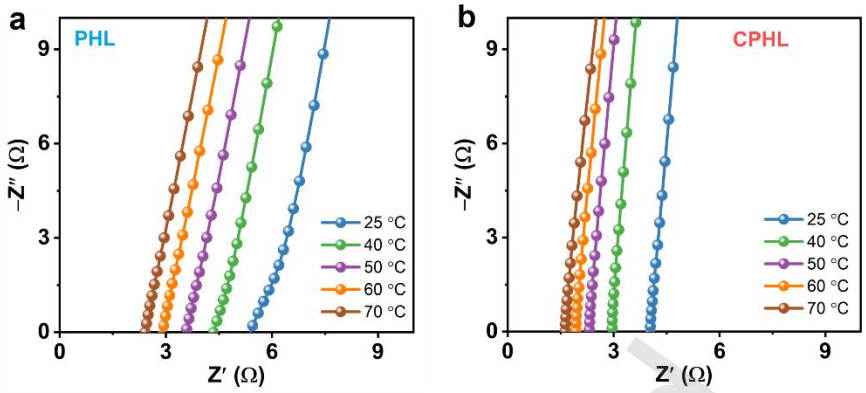

Figure S11 Ionic conductivity of (**a**) PHL and (**b**) CPHL electrolytes at different temperatures.

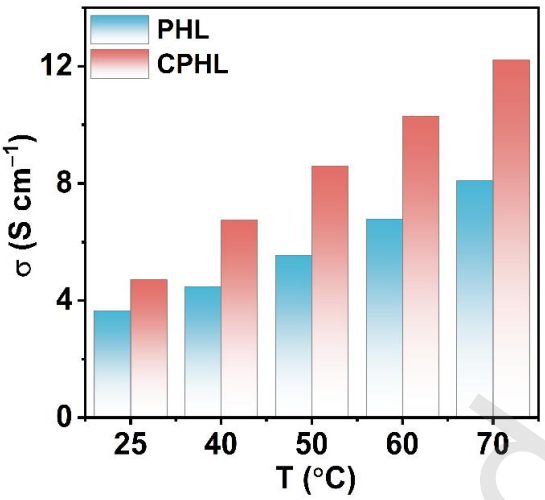

Figure S12 Ionic conductivities of PHL and CPHL at various temperatures.

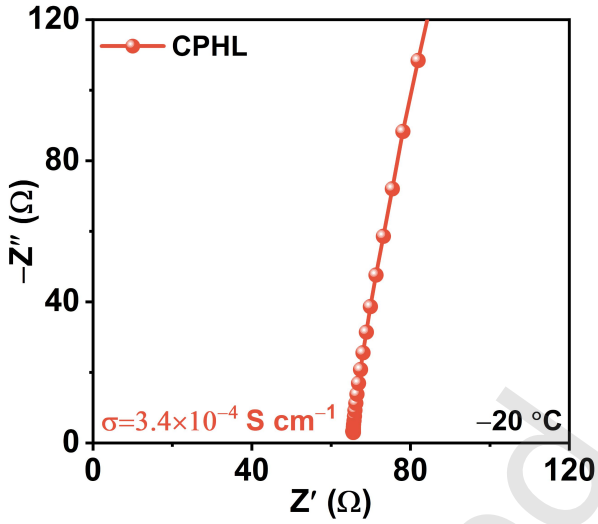

Figure S13 Ionic conductivity of CPHL electrolytes at –20 °C.

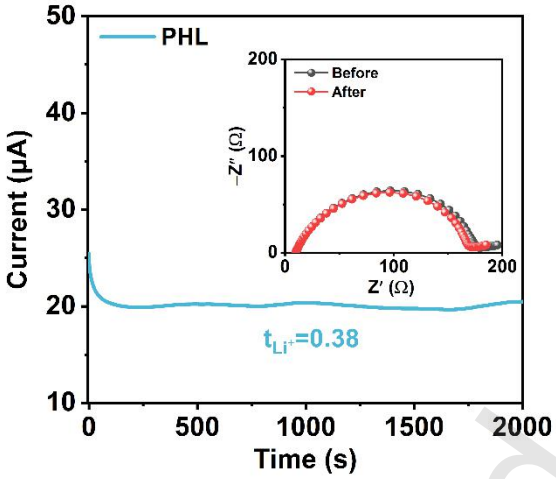

Figure S14 The Li^+ ion transference number of PHL electrolyte.

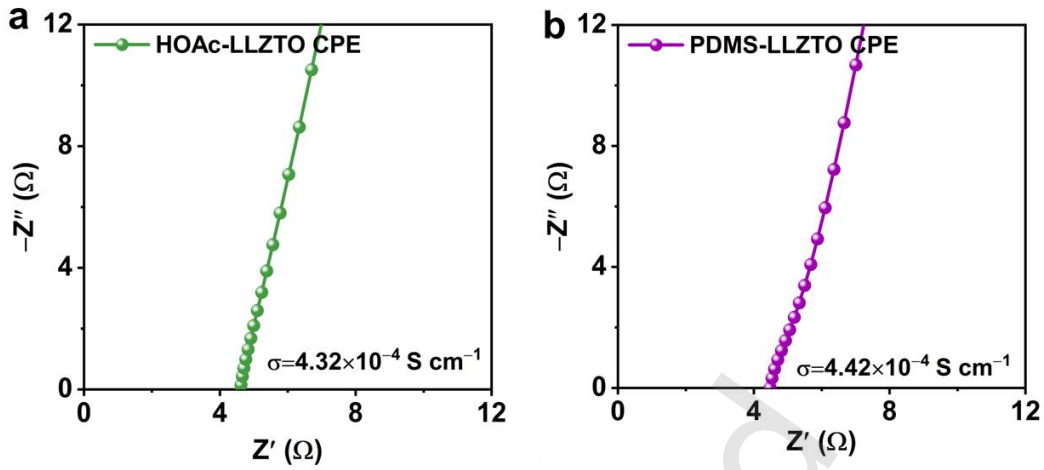

Figure S15 Ionic conductivities of (**a**) acetic acid (HOAc)-LLZTO CPE and (**b**) polydimethylsiloxane (PDMS)-LLZTO CPE at RT.

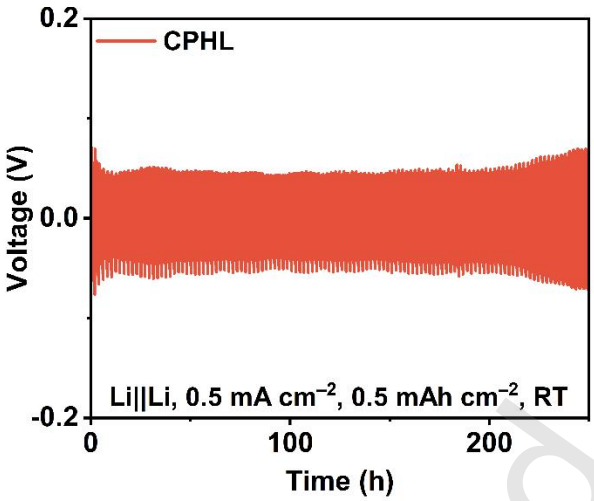

Figure S16 The constant current cycling curves of Li|CPHL|Li symmetric cells at current density of 0.5 mA cm^{-2} and 0.5 mAh cm^{-2}.

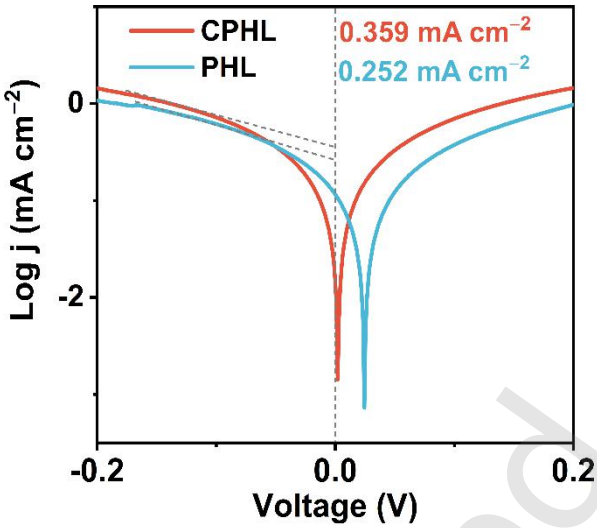

Figure S17 Tafel curves of PHL and CPHL.

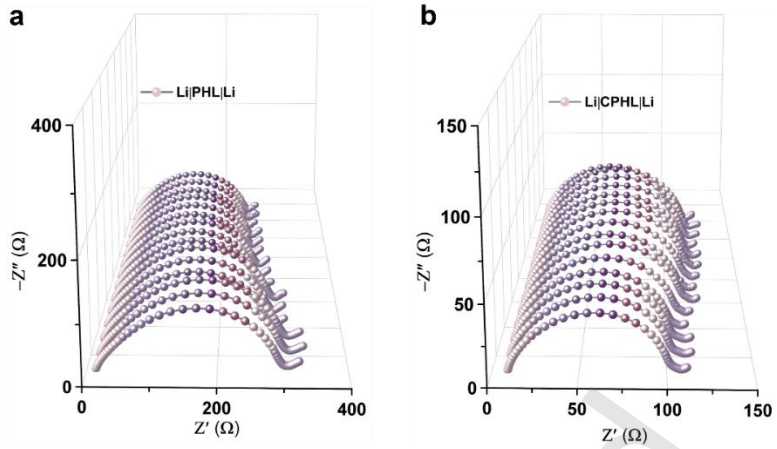

Figure S18 The resistance curves of (**a**) Li|PHL|Li and (**b**) Li|CPHL|Li symmetric cells in 15 cycles.

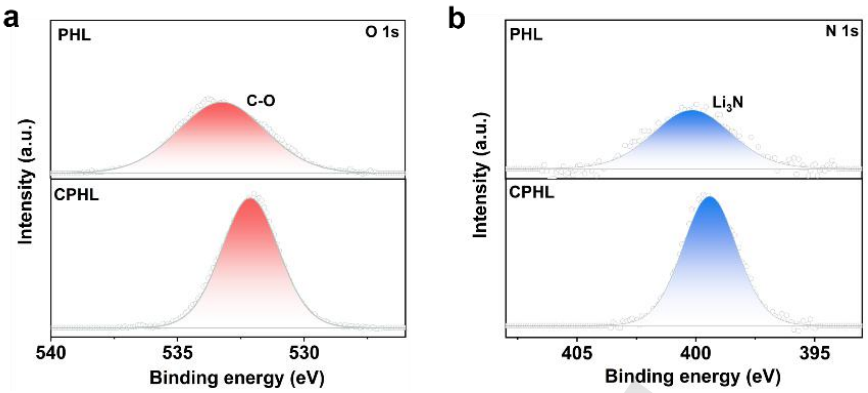

Figure S19 XPS spectra of (**a**) O 1s and (**b**) N 1s of Li anode with different electrolytes.

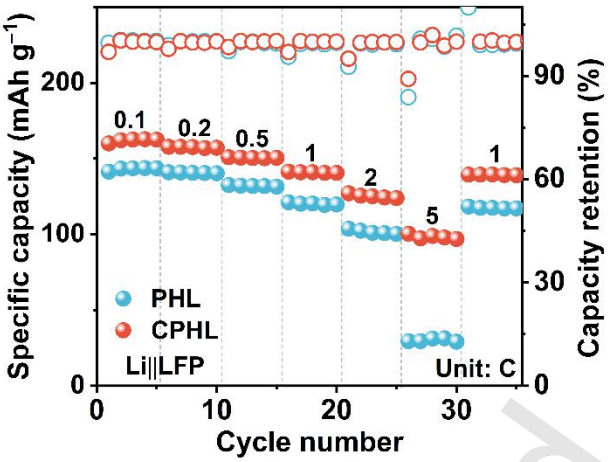

Figure S20 Rate performance of the Li||LFP cells based on PHL and CPHL.

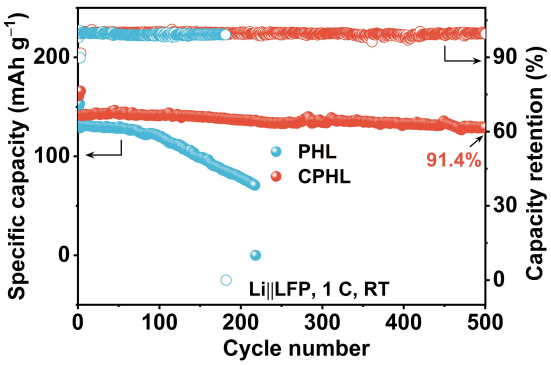

Figure S21 Long-term cycling performance of Li||LFP cells assembled with PHL and CPHL at 1 C and 2.5-3.8 V.

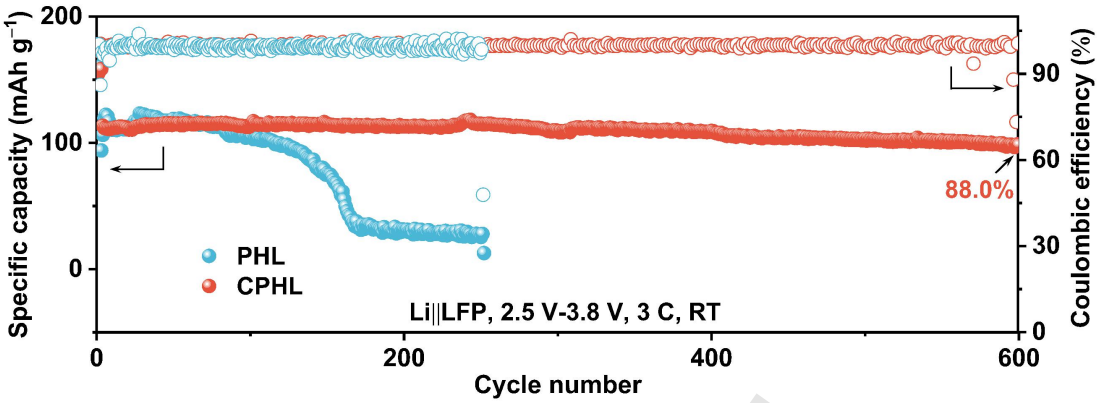

Figure S22 Cycling performance of Li||LFP cells with PHL and CPHL at 2.5 V-3.8 V and 3 C.

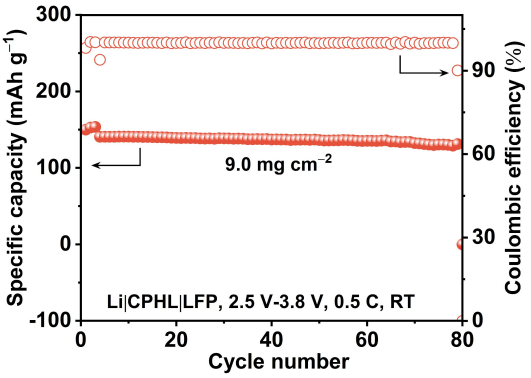

Figure S23 Cycling performance of Li|CPHL|LFP cell with high-cathode loading (9.0 mg cm^{-2}) at 2.5 V-3.8 V and 0.5 C.

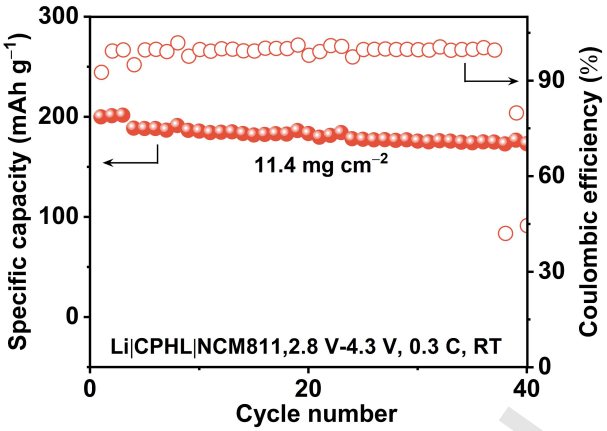

Figure S24 Cycling performance of Li|CPHL|NCM811 cell with high-cathode loading (11.4 mg cm^{-2}) at 2.8 V-4.3 V and 0.3 C.

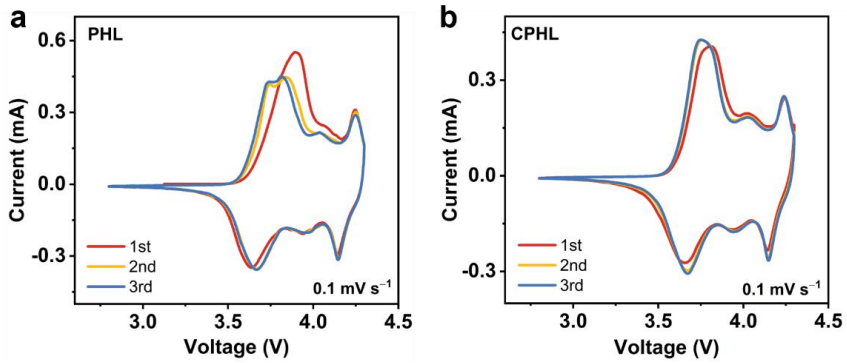

Figure S25 Cyclic voltammetry curves for the first three cycles of (**a**) Li|PHL|NCM811 and (**b**) Li|CPHL|NCM811 cells.

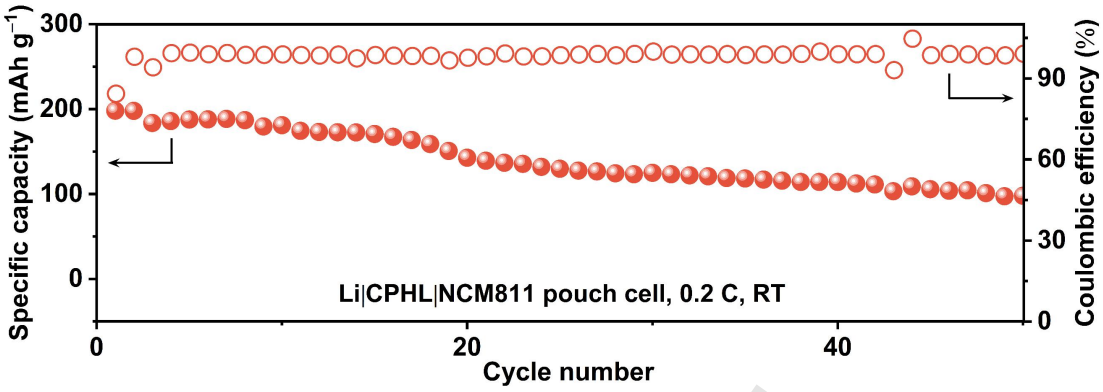

Figure S26 The cycling performance of Li|CPHL|NCM811 pouch cell at 0.2 C.

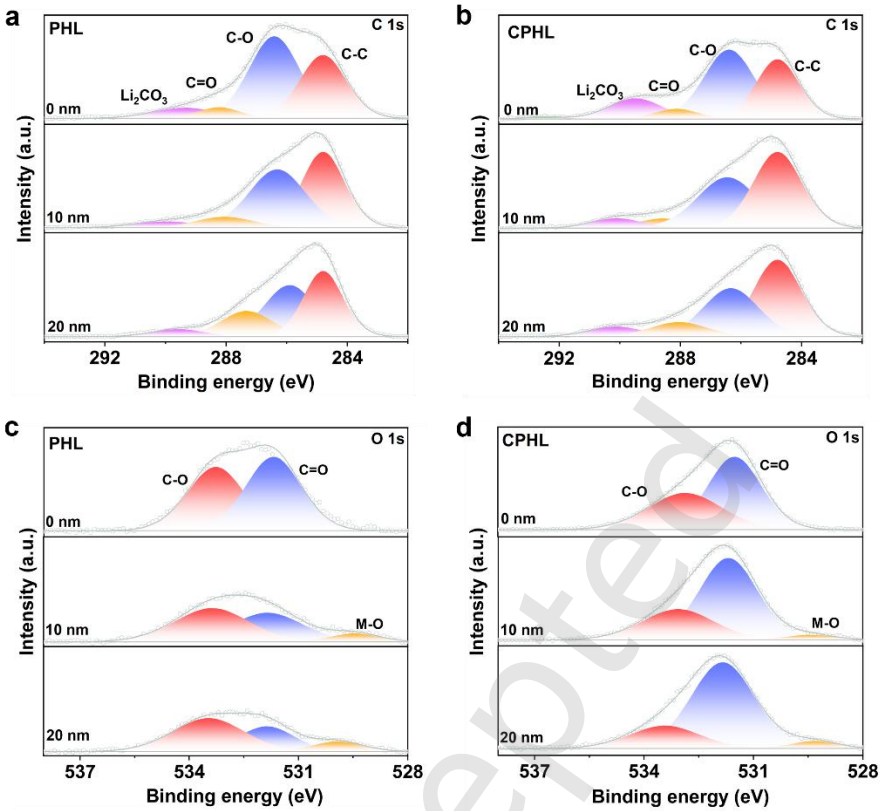

Figure S27 (**a-d**) XPS depth profiles of C 1s and O 1s of cycled NCM811 cathodes with PHL and CPHL.

Supplementary references

[S1] M. Cui, N. Gao, W. Zhao, H. Zhao, Z. Cao et al., Self-regulating interfacial space charge through polyanion repulsion effect towards dendrite-Free polymer lithium-metal batteries. Adv. Energy Mater. **14,** 2303834 (2024). https://doi.org/10.1002/aenm.202303834

[S2] A. D. Becke, Density‐functional thermochemistry. III. The role of exact exchange. J. Chem. Phys. **98,** 5648–5652 (1993). https://doi.org/10.1063/1.464913

[S3] Lee, C. T.; Yang, W. T.; Parr, R. G. Phys. Rev. B: Condens. Development of the Colle-Salvetti correlation-energy formula into a functional of the electron density. Matter Mater. Phys. **37,** 785, (1988). https://doi.org/10.1103/PhysRevB.37.785